

LUDWIG MAXIMILIAN UNIVERSITY OF MUNICH
FACULTY OF PHYSICS

MAX PLANCK INSTITUTE OF QUANTUM OPTICS
DIVISION FOR QUANTUM MANY-BODY SYSTEMS

DESIGNING A 3D MAGNETO-OPTICAL TRAP AND FESHBACH FIELDS FOR A FERMION QUANTUM PROCESSOR

MASTER'S THESIS

supervised by
Prof. Dr. Immanuel Bloch,
Dr. Timon Hiker,
and Dr. Philipp Preiß

December 2022

Tobias Maximilian Philipp Schattauer

LUDWIG-MAXIMILIANS-UNIVERSITÄT MÜNCHEN
FAKULTÄT FÜR PHYSIK

MAX-PLANCK-INSTITUT FÜR QUANTENOPTIK
ABTEILUNG FÜR QUANTEN-VIELTEILCHENSYSTEME

ENTWICKLUNG EINER
 ^3D -MAGNETO-OPTISCHEN FALLE UND
VON FESHBACH-FELDERN FÜR EINEN
FERMIONISCHEN QUANTENPROZESSOR

MASTERARBEIT

betreut von
Prof. Dr. Immanuel Bloch,
Dr. Timon Hiker
und Dr. Philipp Preiß

Dezember 2022

Tobias Maximilian Philipp Schattauer

Abstract

Abstract goes here...

Contents

1. Introduction	5
2. FermiQP: a Fermion Quantum Processor	6
3. The 3-dimensional Magneto-optical Trap	7
3.1. Theory of Laser Cooling with Magneto-optical Traps and Gray Molasses	7
3.2. Preparation of the Trap Laser Light	21
3.3. Projected Implementation	31
4. Feshbach and Gradient Field Coils	43
4.1. Requirements and Constraints	43
4.2. Simulation	48
4.3. Coil Properties	52
4.4. Field Characterization	58
A. The Jones and Azimuth-Ellipticity Polarization Bases	64
B. Coil simulation library	65
C. Rules of Thumb for Magnetic Fields and Gradients	66
References	69

1. Introduction

2. FermiQP: a Fermion Quantum Processor

3. The 3-dimensional Magneto-optical Trap

This chapter presents the design and planning of the 3-dimensional magneto-optical trap and the gray molasses of the FermiQP demonstrator. First, the theory of laser cooling with these two techniques is recapitulated. Subsequently, the implementation of the joint laser setup for both magneto-optical traps and the gray molasses is explained. Afterwards, the projected realization of the magneto-optical trap is described, covering the geometry, the optics for the trapping light, and the magnetic gradients. It concludes with some estimations of key trap properties.

Due to massive supply chain problems and delivery time extensions during this thesis project, only the trap laser setup and the magnetic gradient coils could be put into operation and characterized during the writing of this thesis. Due to the lack of an assembled and depressurized experiment chamber, the trap itself has not yet been built.

3.1. Theory of Laser Cooling with Magneto-optical Traps and Gray Molasses

Laser light exerting a force onto an atom is the underlying mechanism of laser cooling. There are different implementations, each one making use of a different way light can interact with atoms: Doppler-cooling techniques on the one hand, which are used in, among others, magneto-optical traps, make use of momentum transfer from absorbed photons and are limited regarding the achievable temperature by spontaneous decays. Sub-Doppler-cooling techniques, on the other hand, surpass this limit using other ways of atom-light interaction, such as the optical dipole trap, Raman sideband cooling or Sisyphus cooling [1].

The following explanations of the theory of magneto-optical traps follow the respective chapters in [1] and [2].

Light scattering on atoms

Electromagnetic waves carry momentum $\vec{p} = \hbar \vec{k}$, which is directed into their propagation direction and depends on their wavelength $\lambda = \frac{2\pi}{k}$. When laser light scatters on atoms, a momentum transfer between the photons of the laser and the atoms takes place. The total transfer can be broken down

3. The 3-dimensional Magneto-optical Trap

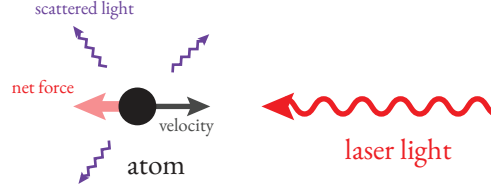


Figure 3.1.: Schematic of momentum transfer from the laser to the atom moving against the laser propagation direction: The momenta of the scattered photons, originating from spontaneous in random directions, average to zero, leading to a net decelerating force over many scattering events.

into two parts: the absorption of laser photons where the atoms acquire momentum $\hbar\vec{k}$ per photon, and the spontaneous emission of photons where the atoms lose $\hbar\vec{k}_{\text{emitted}}$ per photon:

$$\vec{p}_{\text{after}} = \vec{p}_{\text{before}} + \hbar\vec{k} + \hbar\vec{k}_{\text{emitted}} \quad (3.1)$$

While the former is always aligned with the laser beam, the latter averages to zero over many scattering events as photons are emitted into random directions. In this way, atoms lose momentum over many scattering events if the propagation of the light and the atom movement are in opposite directions:

$$\langle \vec{p}_{\text{after}} - \vec{p}_{\text{before}} \rangle = \langle \hbar\vec{k} \rangle + \underbrace{\langle \hbar\vec{k}_{\text{emitted}} \rangle}_{=0} \quad (3.2)$$

As visualized in figure 3.1, the atoms are decelerated opposite the direction of laser propagation, corresponding to cooling of the atoms.

The rate at which this happens is determined by the fraction ρ_{ee} of atoms in the excited state and the rate Γ at which they spontaneously decay into the ground state emitting a photon:

$$R_{\text{scatter}} = \Gamma\rho_{ee} \quad (3.3)$$

The scattering force, which corresponds to the decrease of momentum of the atoms averaged over many scattering events, is hence

$$\vec{F}_{\text{scatter}} = R_{\text{scatter}}\hbar\vec{k} = \Gamma\rho_{ee}\hbar\vec{k}. \quad (3.4)$$

The light-atom interaction process can be described semi-classically understanding the light as a classical electromagnetic wave, but describing the dynamics within the atom using the quantum mechanical optical Bloch equations, according to which the steady-state population of the excited state amounts to

$$\rho_{ee} = \frac{s_0/2}{1 + s_0 + \left(\frac{2\delta}{\Gamma}\right)^2}, \quad (3.5)$$

3. The 3-dimensional Magneto-optical Trap

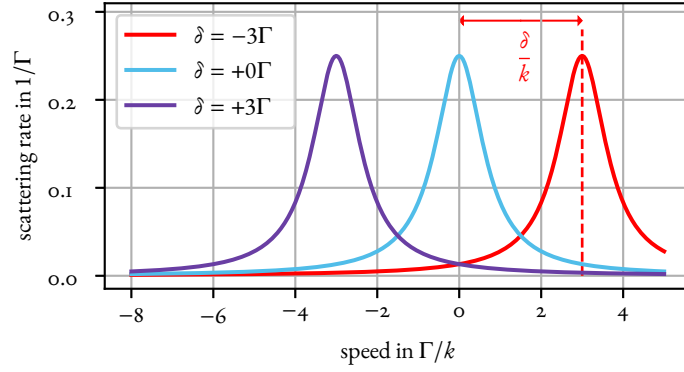


Figure 3.2.: Scattering rate R_{scatter} as a function of the atom speed against the laser direction for different values of the detuning δ_{laser} : Scattering is maximal where the Doppler shift compensates the detuning, thus $v = \frac{\delta}{k}$

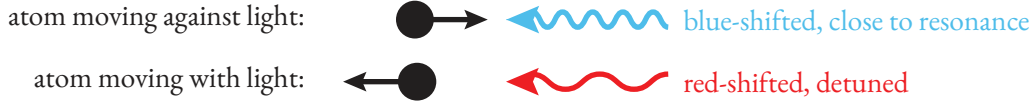


Figure 3.3.: Atoms moving against the direction of laser propagation see the laser light blue-shifted, atoms moving in the other direction see it red-shifted. For negative laser detuning ($\delta_{\text{laser}} < 0$) the former sense the light as it appears to be close to resonance, the latter do not sense it because it is far detuned for them.

with the saturation parameter $s_0 = \frac{I}{I_s} = \frac{2\Omega^2}{\Gamma^2}$, the Rabi frequency $\Omega \propto \sqrt{I}$, and the detuning δ . The detuning is the deviation of the laser frequency from the transition frequency, as seen by the atom taking into account the Doppler shift stemming from its velocity \vec{v} with respect to the propagation direction \vec{k} of the laser:

$$\delta = \underbrace{\omega_{\text{laser}} - \vec{k}\vec{v}}_{\text{apparent laser frequency}} - \omega_{\text{transition}} = \omega_{\text{laser}} - \omega_{\text{transition}} \pm kv \cos \theta \quad (3.6)$$

where + is for atoms moving against and – for atoms moving along with the laser. θ is the angle between the atoms' velocity and the propagation direction of the light.

Figure 3.2 shows how the scattering rate and thus also the scattering force depends on the velocity of the atoms. The force is maximal for velocities where the Doppler shift cancels out the laser detuning: $\vec{k}\vec{v} = \omega_{\text{laser}} - \omega_{\text{transition}}$. Deceleration of atoms happens with red laser detuning $\delta_{\text{laser}} < 0$ as the light is resonant for atoms moving against the laser propagation direction. These atoms sense the light scattering force against their direction of movement. Atoms moving in the other direction do not sense the scattering force as for them the laser is too far detuned (see figure 3.3).

3. The 3-dimensional Magneto-optical Trap

Doppler limit While the momentum gained by spontaneous emission of photons averages to zero, the square of momentum $\vec{p}_{\text{after decay}}^2$ gained from the spontaneous decays does not. This means that the atom is always left with a finite amount of kinetic energy from the recoil of emitted photons. The magnitude of this leftover energy is related to the decay rate Γ and is called the Doppler limit:

$$k_B T_D = \frac{\hbar \Gamma}{2} \quad (3.7)$$

Laser cooling techniques using spontaneous emission of photons, by principle, cannot provide cooling below this limit (neglecting any coincidental sub-Doppler cooling effects) [1].

Magneto-optical Traps

Magneto-optical traps use light scattering on atoms in order to cool and spatially confine atoms. They have become a standard tool in ultracold neutral atom experiments over the last decades.

Optical molasses Magneto-optical traps make use of the optical molasses technique for slowing down atoms. As discussed above, light scattering provides a decelerating force opposite the direction of laser beams in case of red detuning. By using three pairs of counter-propagating laser beams, one pair in each spatial degree of freedom, atoms are decelerated in each direction. For an atom of speed v , travelling at an angle θ with respect to the counter-propagating beams with wave number k , the scattering force of two counter-propagating beams adds up to

$$F_{\text{OM}} = F_{\text{scatter}}(\omega_{\text{laser}} - \omega_{\text{transition}} - kv \cos \theta) - F_{\text{scatter}}(\omega_{\text{laser}} - \omega_{\text{transition}} + kv \cos \theta). \quad (3.8)$$

For slow velocities $v \ll \frac{\Gamma}{k}$, the force can be linearized as a friction force:

$$F_{\text{OM}} \approx -2 \frac{\partial F_{\text{scatter}}}{\partial \omega} kv \cos \theta \equiv -(\alpha \cos \theta) v \quad (3.9)$$

with damping $\alpha = 2k \frac{\partial F}{\partial \omega} = -8\hbar k^2 s_0 \frac{\delta/\Gamma}{(1+s_0+(2\delta/\Gamma)^2)^2}$ where low saturation $s_0 \ll 1$ is assumed [1, 2]. The velocity-dependence of the optical molasses deceleration force is depicted in figure 3.4. Slow atoms don't sense a net force whereas moving atoms are decelerated as they compensate the detuning of the light with the Doppler shift. For detunings $\delta \approx -0.5\Gamma$, the maximum of the force is approximately at the resonance speed, thus at $v \approx \pm \frac{\delta}{k}$.

Spatial confinement For spatial confinement of atoms, the Zeeman effect is exploited. It shifts the energy levels of magnetic sublevels of spin or orbital angular momentum states at presence of an external magnetic field. This energy shift (with respect to a situation without a magnetic field, where the magnetic sublevels are degenerate) amounts to

$$\Delta E(m) = g\mu_B m B \quad (3.10)$$

3. The 3-dimensional Magneto-optical Trap

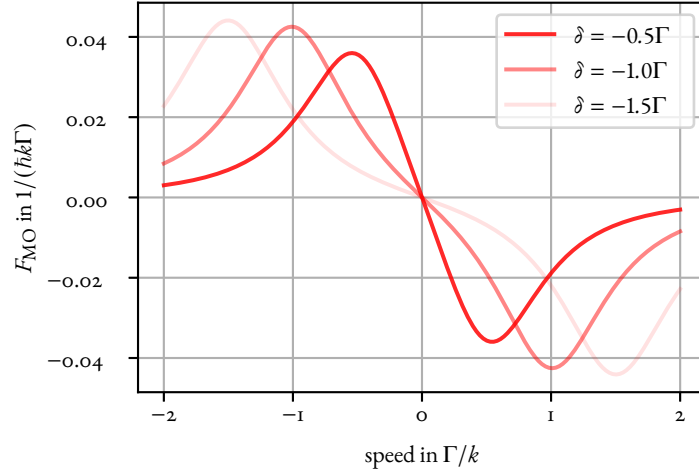


Figure 3.4.: Optical molasses force F_{MO} as a function of velocity for different detunings, as in (3.8): Due to the Doppler shift, fast atoms are close to resonance and sense the scattering force whereas slow atoms don't sense a net force. For detunings of $\delta \approx -0.5\Gamma$, the maximum force is at $v \approx \frac{\delta}{k}$.

with the Landé factor $g \approx 2$, the Bohr magneton μ_B , the magnetic field B and the magnetic quantum number m . When applying a magnetic gradient, the transition frequency between two magnetic sublevels m and $m + 1$ becomes dependent on the position q ¹:

$$\begin{aligned} \omega_{\text{transition}}(q) &= \omega_{\text{transition}} + \frac{\Delta E(q)}{\hbar} \\ &= \omega_{\text{transition}} + \frac{g\mu_B}{\hbar} \frac{\partial B}{\partial q} q \equiv \omega_{\text{transition}} + \beta q \end{aligned} \quad (3.11)$$

Hence also the detuning between the laser light and the driven transition becomes position-dependent which allows for spatially varying scattering forces.

In order to create a confining trap, laser beams and magnetic gradients are calibrated such that the atoms sense restoring forces towards a center point when they are displaced from there. This means that on opposite sides of the trap, these restoring forces must point in opposite directions. One achieves this by clever use of the magnetic gradient and the polarization-dependent selection rules for transitions between magnetic sublevels, as visualized in figures 3.5 and 3.6:

- Due to the magnetic gradient, the magnetic field has different sign on opposite sides of the trap center, hence also the Zeeman shifts ΔE have different sign for the transitions $\Delta m = +1$ and $\Delta m = -1$. This also means that on each side only one of these transitions is close to resonance with the laser light.

¹In the following paragraphs, q will be used as a generalized coordinate. In the setup of the FermiQP demonstrator, setting $q = x$ would condition the following considerations to the atomic beam axis (x).

3. The 3-dimensional Magneto-optical Trap

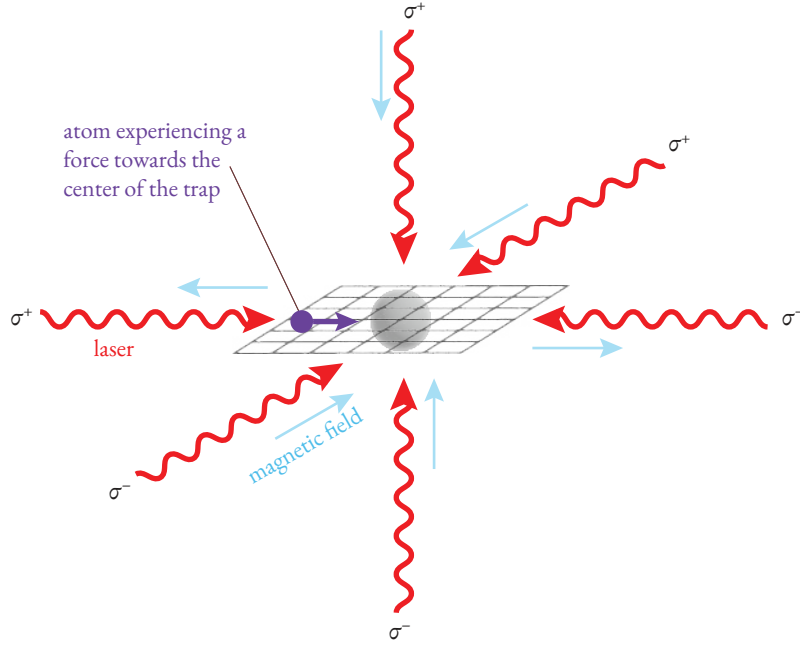


Figure 3.5.: Restoring mechanism in a 3-dimensional magneto-optical trap: Pairs of counter-propagating laser beams in each spatial degree of freedom exert restoring forces on atoms displaced from the center. Setting the beams' circular polarization such that it has σ^+ helicity where the magnetic field points against the quantization axis and σ^- helicity where the magnetic field points along the quantization axis ensures that the force is always directed towards the center. See also figure 3.6.

- σ^+ light (light with right helicity with respect to the atoms' quantization axis) can only drive transitions with $\Delta m = +1$, σ^- light (left helicity) can only drive transitions with $\Delta m = -1$. In each pair of counter-propagating beams, one of the beams has σ^+ and one has σ^- polarization, such that on each side the atoms only see the beam propagating towards the trap center.

Note that the helicity of the polarization is given with respect to the (arbitrary, but fixed) quantization axis of the atoms. As the laser beams in each pair counter-propagate, one of them points in and the other one against the direction the quantization axis. The circular polarization with respect to their respective propagation direction is hence the same for both laser beams in a pair (both |R) or both |L), depending on the direction of the gradient field).

Similarly to the optical molasses consideration, in the magneto-optical trap the scattering forces can be linearized for small displacements $q \ll \frac{\Gamma}{\beta}$ (here again for one dimension) [1]:

$$\begin{aligned}
 F_{\text{MOT}} &= F_{\text{scatter}}^{\sigma^+}(\omega_{\text{laser}} - \omega_{\text{transition}}(q) - kv \cos \theta) + F_{\text{scatter}}^{\sigma^-}(\omega_{\text{laser}} - \omega_{\text{transition}}(q) + kv \cos \theta) \\
 &\approx -2 \frac{\partial F_{\text{scatter}}}{\partial \omega} k \cos \theta v + 2 \frac{\partial F_{\text{scatter}}}{\partial \omega_0} \beta q \equiv -(\alpha \cos \theta) v - \frac{\alpha \beta}{k} q
 \end{aligned} \tag{3.12}$$

3. The 3-dimensional Magneto-optical Trap

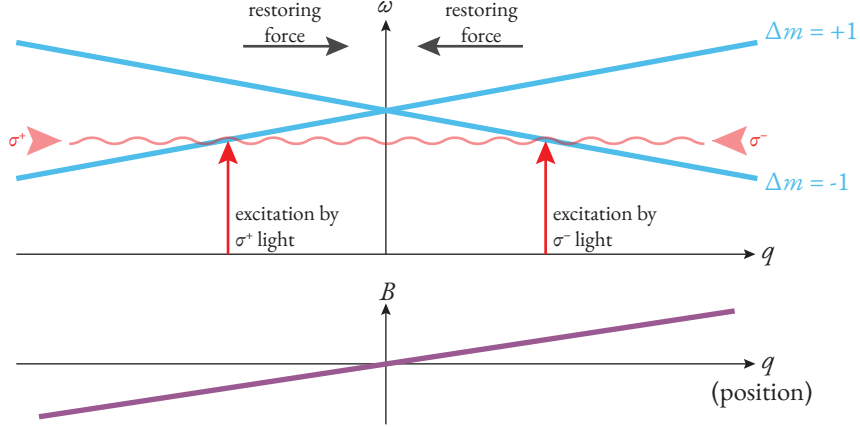


Figure 3.6.: Details of the restoring mechanism in a magneto-optical trap: On both sides of the trap different transitions between magnetic sublevels are resonant with the red-detuned trap light. Due to the polarization-dependent selection rules, only the beam pointing towards the center can drive the transition on each side. E.g. on the left, the $\Delta m = +1$ transition is closer to resonance. Only the σ^+ light coming from the left can drive this transition, hence atoms displaced to the left of the trap only acquire momentum towards the trap center.

This demonstrates again that a magneto-optical trap combines the friction force $-(\alpha \cos \theta)v$ for slowing down atoms and the trapping force $-\frac{\alpha\beta}{k}q$ confining the atoms to a trap center.

Relevant transitions in alkali atoms For cooling alkali atoms in a magneto-optical trap, transitions between electronic levels J_g and $J_g + 1$ are used for scattering (g for ground state). The cooling transition can be implemented between hyperfine states $|J = J_g, F = J_g + I\rangle$ (the highest F in the J_g manifold), and $|J = J_g + 1, F = J_g + I + 1\rangle$. This ensures that all decays, owing to the selection rule $\Delta F \in \{-1, 0, 1\}$, bring the atom down into the original $|J = J_g, F = J_g + I\rangle$ state such that the cooling cycle can start from anew.

If, however, the atom is excited into the $|J = J_g + 1, F = J_g + I\rangle$ state due to a non-zero matrix element for this transition, it can also fall back into the $|J = J_g, F = J_g + I - 1\rangle$ state. In this case, it would not be subject to cooling anymore as this state is dark to the cooling transition. To combat this, a repumper laser beam is shone in addition to the cooler beam. This beam addresses the transition $|J = J_g, F = J_g + I - 1\rangle \rightarrow |J = J_g + 1, F = J_g + I\rangle$ from where they can decay back into the ground state of the cooling transition which returns them into the cooling cycle [2].

The cooling and repumping mechanism is illustrated in figure 3.7, the respective cascades can be sum-

3. The 3-dimensional Magneto-optical Trap

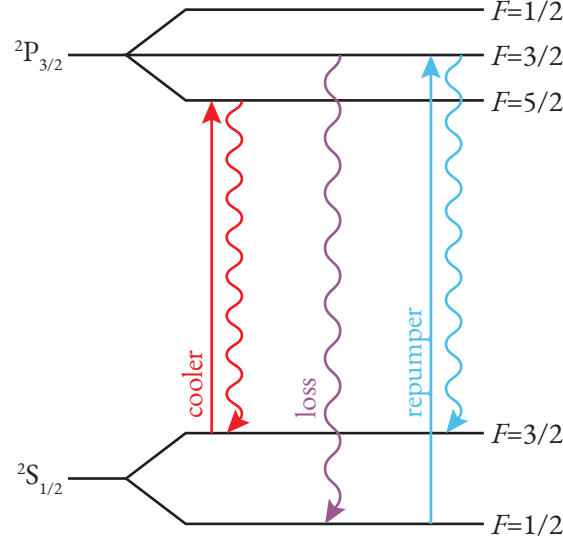


Figure 3.7.: Schematic of the cooling and repumping scheme in an alkali atom, here exemplarily for fermionic ${}^6\text{Li}$ atoms ($I = 1, J_g = \frac{1}{2}$): The cooling cycle is $|\frac{1}{2}, \frac{3}{2}\rangle \rightarrow |\frac{3}{2}, \frac{5}{2}\rangle \rightsquigarrow |\frac{1}{2}, \frac{3}{2}\rangle$. Atoms are lost if, during cooling, they end up in the $|\frac{3}{2}, \frac{3}{2}\rangle$ state and decay down into the $|\frac{1}{2}, \frac{1}{2}\rangle$ state. The repumper then leads them back into the cooling cycle via $|\frac{1}{2}, \frac{1}{2}\rangle \rightarrow |\frac{3}{2}, \frac{3}{2}\rangle \rightsquigarrow |\frac{1}{2}, \frac{3}{2}\rangle$. As in ${}^6\text{Li}$ the ${}^2\text{P}_{3/2}$ manifold is not resolved for the cooler transition, the loss decay happens very often, and the rates of cooling and repumping are on the same order of magnitude.

marized as

$$\text{cooling: } |J_g, J_g + I\rangle \xrightarrow{\text{cooler}} |J_g + 1, J_g + I + 1\rangle \rightsquigarrow |J_g, J_g + I\rangle \quad (3.13)$$

$$\text{repumping: } |J_g + 1, J_g + I\rangle \rightsquigarrow_{\text{loss}} |J_g, J_g + I - 1\rangle \xrightarrow{\text{repumper}} |J_g + 1, J_g + I\rangle \rightsquigarrow |J_g, J_g + I\rangle \quad (3.14)$$

with notation in the $|J, F\rangle$ basis.

Characteristic Quantities and Benchmarks Important technical quantities that can be adjusted for optimizing the performance of a MOT include:

- laser intensity saturations $s_{0,\text{cooler}}$ and $s_{0,\text{repumper}}$
- laser detunings with respect to the transition wavelength δ_{cooler} and δ_{repumper}
- the angle θ of the atomic beam with respect to the cooling laser beams
- magnetic gradient $\frac{\partial B}{\partial q}$

3. The 3-dimensional Magneto-optical Trap

These quantities might also be varied over one trapping cycle, e.g. for compressing the trap and cooling the atoms further down by increasing the magnetic gradient and decreasing the laser intensity as well as the laser detuning.

A magneto-optical trap can be characterized by, among others, the following quantities:

- The radius r_{trap} of the trapping region where the atoms are slowed is on the order of the size of the trapping beams: $r_{\text{trap}} \approx w$ (beam waist radius).
- One can estimate a maximum velocity $v_{\text{max, capture}}$ such that the atoms entering the trap are decelerated to standstill within the length $2r_{\text{trap}}$ of the trap. This would require that their kinetic energy $\frac{1}{2}mv^2$ be dissipated by the cooling force performing the mechanical work $\int F_{\text{MOT}}(q) dq$. In case of high radiation pressure, this can be approximated with the maximum scattering force $F_{\text{scatter, max}}(q) = \frac{\hbar k \Gamma}{2}$ being constant over the whole trap, leading to the following capture velocity [3]:

$$v_{\text{capture, max}}^{\text{high}} \approx \sqrt{\frac{\hbar k \Gamma \cdot 2r_{\text{trap}}}{m}}. \quad (3.15)$$

For a lower scattering force ($s_0 \ll 1$), the work is $\int F_{\text{MOT}}(q) dq = \int (-\alpha \cos \theta v(q) - \frac{\alpha \beta}{k} q) dq = - \int \alpha \cos \theta v(q) dq$ (see equation 3.12):

$$v_{\text{max, capture}}^{\text{low}} = \sqrt{\frac{2}{m} \int_{-r_{\text{trap}}}^{+r_{\text{trap}}} F_{\text{MOT}}(q) dq} \approx \sqrt{\frac{2}{m} \alpha \cos \theta \cdot \frac{v_{\text{max, capture}}}{2} \cdot 2r_{\text{trap}}} \quad (3.16)$$

where the integral over the velocity was estimated as $\int_{-r_{\text{trap}}}^{+r_{\text{trap}}} v(q) dq \approx \frac{v_{\text{max}}}{2} \cdot 2r_{\text{trap}}$, assuming that the velocity in the trap is reduced at a constant rate until standstill. The capture velocity is then estimated as

$$v_{\text{max, capture}}^{\text{low}} \approx \frac{2\alpha \cos \theta r_{\text{trap}}}{m}. \quad (3.17)$$

Figure 3.8 compares the two estimations of the capture velocity. For small saturation intensities, $v_{\text{max, capture}}^{\text{low}}$ takes into consideration that the slowing force is weak, hence only slow atoms can be brought to standstill in the trap. For higher saturation intensities, where it loses applicability, $v_{\text{max, capture}}^{\text{low}}$ approaches $v_{\text{max, capture}}^{\text{high}}$ which is an upper bound of the capture velocity.

- For atoms of velocity v , the trap size is also set by the distance $r_{\text{resonance}}$ from the trap center where the trapping beams are resonant due to the Zeeman shift,

3. The 3-dimensional Magneto-optical Trap

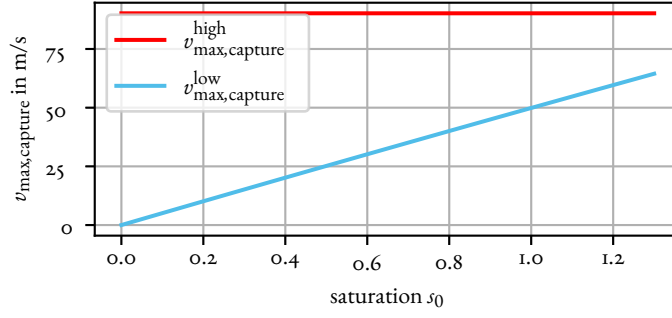


Figure 3.8.: Comparison between the different estimations of the capture velocity: The low-intensity capture velocity $v_{\text{max,capture}}^{\text{low}}$ takes the low scattering force at $s_0 \ll 1$ into consideration, approaching the intensity-ignorant upper-bound capture velocity $v_{\text{max,capture}}^{\text{high}}$ around $s_0 \approx 1$. Parameters: $\delta = -5\Gamma$, $r_{\text{trap}} = 7 \text{ mm}$, $\theta = 0^\circ$.

i.e. $\omega_{\text{laser}} - \omega_{\text{transition}} - \vec{k}\vec{v} = \frac{g\mu_B}{\hbar} \frac{\partial B}{\partial q} r_{\text{resonance}}$, from which follows [4]

$$r_{\text{resonance}}(\vec{v}) = \frac{\hbar}{g\mu_B} \left(\frac{\partial B}{\partial q} \right)^{-1} \left((\omega_{\text{laser}} - \omega_{\text{transition}}) - \vec{k}\vec{v} \right). \quad (3.18)$$

At larger distances from the trap, the trapping light is blue detuned (see figure 3.6) and thus not decelerating, hence slowing of atoms of velocity \vec{v} only occurs within a distance of $r_{\text{resonance}}(\vec{v})$. In a one-dimensional consideration with $\vec{k}\vec{v} = -kv \cos \theta$, one can deduce a maximum speed at which atoms entering the trap can still be on resonance at the outermost displacement r_{trap} [4]:

$$v_{\text{max, resonance}} \approx \frac{1}{k \cos \theta} \left(\frac{g\mu_B}{\hbar} \frac{\partial B}{\partial q} r_{\text{trap}} - (\omega_{\text{laser}} - \omega_{\text{transition}}) \right) \quad (3.19)$$

Assuming that the slowing force is large, one can assume that, on the way towards the trap center, the atoms are kept on resonance with the (due to the magnetic gradient) ever less detuned trapping light. In this case, $v_{\text{max, resonance}}$ can also give the order of magnitude of the capture velocity of the trap [4].

- The loading rate characterizes how many atoms can be trapped per time unit. It depends on the trap geometry, the flux rate and the velocity distribution of the incoming atoms, the applied gradients, laser powers, detunings of the cooling and repumping light, collisions among the trapped atoms, and many more. Due to these complex dependencies, the loading rate needs to be characterized experimentally.
- The temperature of the atoms in the trap. It is usually in the order of magnitude above the Doppler temperature T_D and also depends on a multitude of parameters.
- Regarding the trap as a harmonic oscillator, one can quantify the atom oscillation frequency $\omega_{\text{MOT}} = \frac{\alpha}{m}$, oscillation damping rate $\Gamma_{\text{MOT}} = \sqrt{\frac{\alpha\beta}{km}}$, and atom trap restoring time $t_{\text{restore}} =$

3. The 3-dimensional Magneto-optical Trap

$\frac{2\Gamma_{\text{MOT}}}{\omega_{\text{MOT}}^2}$ with the atom mass m [2].

Magneto-optical Traps with Lithium Magneto-optical traps for lithium usually operate on the D₂ line, i.e. between the $^2S_{1/2}$ and $^2P_{3/2}$ manifolds, as in the implementation in the FermiQP demonstrator. Since the first implementation with lithium in the early 1990s [5], they have become a standard part of ultracold lithium experiments, namely for experiments with fermionic [6, 7] and bosonic [5, 8] lithium as well as for isotope mixtures [9–12] and species mixtures [4, 13, 14].

For D₂ line traps for fermionic lithium, the energy splitting between the two ground state hyperfine manifolds $|J = 1/2, F = 1/2\rangle$ and $|J = 1/2, F = 3/2\rangle$ is 228 MHz, which sets the order of magnitude for the difference in frequency of the cooler and repumper laser beams. The cooler addresses the transition $|^2S_{1/2}, F = 3/2\rangle \rightarrow |^2P_{3/2}\rangle$, the repumper addresses the transition $|^2S_{1/2}, F = 1/2\rangle \rightarrow |^2P_{3/2}\rangle$, as shown in figure 3.9.

It is important to note that the hyperfine levels $F = \frac{5}{2}, \frac{3}{2}$, and $\frac{1}{2}$ of the excited state cannot be resolved because the D₂ line is broader ($\Gamma = 5.87$ MHz) than the splitting between these hyperfine states (4.4 MHz) [15]. This implies that it cannot be controlled which hyperfine state the cooler excites the atoms into. A large fraction of them will hence drop into the $|J = 1/2, F = 1/2\rangle$ state and need to be repumped back into the cycle. For this reason, the cooler and repumper roughly have equal importance in a Lithium magneto-optical trap and should thus also have on comparable power. Another implication is that coincidental sub-Doppler cooling, as observed in magneto-optical traps for other atomic species, cannot be expected to support the cooling process [16].

Typical parameter ranges for 3-dimensional traps with lithium from earlier experiments are [4, 5, 8, 9, 11–14, 17, 18]:

- laser intensities: from a few up to more than 10 saturation intensities, with a little less power on the repumper
- beam diameter: 5 mm to 15 mm
- detuning: mostly around -5Γ , also up to -8Γ ([18]), with the repumper often being less detuned than the cooler
- magnetic gradients: $10 \frac{\text{G}}{\text{cm}}$ to $50 \frac{\text{G}}{\text{cm}}$
- achieved temperature: on the order of 1×10^{-3} K to 3×10^{-4} K
- atom number: about 10^7 to 10^8

Lower temperatures than in magneto-optical traps operating on the D₂ line have been reached by using a UV transition [6, 7] which, however, requires expensive laser sources optical components [17]. More efficient loading rates have been achieved in a magneto-optical trap by adding frequency sidebands onto the cooling light in order to address more velocity classes [18].

3. The 3-dimensional Magneto-optical Trap

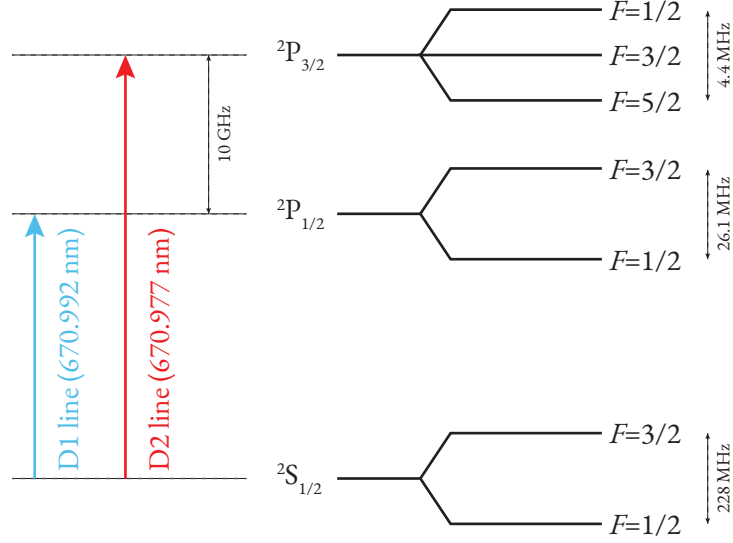


Figure 3.9.: Level diagram of fermionic lithium (${}^6\text{Li}$) [15, 19]: The transition between the ${}^2\text{S}_{1/2}$ and the ${}^2\text{P}_{1/2}$ manifolds is called D₁ line with a frequency of 670.992 MHz. The transition between the ${}^2\text{S}_{1/2}$ and the ${}^2\text{P}_{3/2}$ manifolds is called D₂ line with a frequency of 670.977 MHz. Both have a linewidth of $\Gamma = 5.87$ MHz which means that the ${}^2\text{P}_{3/2}$ manifold cannot be resolved with D₂ light. The hyperfine splitting in the ${}^2\text{S}_{1/2}$ manifold is 228 MHz.

Gray Molasses Cooling

The subsequent step in the cooling cycle in the FermiQP demonstrator, after the 3-dimensional magneto-optical trap, is gray molasses cooling [20, 21]. This sub-Doppler cooling technique operates on the D₁ line of lithium, i.e. the ${}^2\text{S}_{1/2} \rightarrow {}^2\text{P}_{1/2}$ transition [17].

Gray molasses is based on atoms moving in a polarization-gradient field where they move up a potential hill until they decay into a lower energy state, similar to Sisyphus cooling [1]. Gray molasses operates on $\Delta J = 0$ transitions, as is the case for the D₁ line. This transition functions as a Λ -system with the two ground states being the states $|\text{ground}, m\rangle$ and $|\text{ground}, m+2\rangle$ and the excited state being $|\text{excited}, m+1\rangle$ [21], as illustrated in figure 3.10. Coupling between these states is polarization-dependent due to dipole selection rules.

The counter-propagating gray molasses beams have orthogonal polarization, e.g. circular polarization with different helicity. At every point, the superposition of the polarization states of both beams yields an effective polarization sensed by the atoms. This effective polarization depends on the phase of the two light beams with respect to each other, which means that the atoms see alternating circular, elliptical, linear, elliptical, etc. polarization along their journey through the light field. This makes the coupling between the relevant states position-dependent, as hinted at in figure 3.11.

In the gray molasses' light field, the Λ -system is dressed with two orthogonal, hence not mutually coupling, eigenstates $|C\rangle$ and $|D\rangle$, being superpositions of the two ground states. One of them, $|C\rangle$, cou-

3. The 3-dimensional Magneto-optical Trap

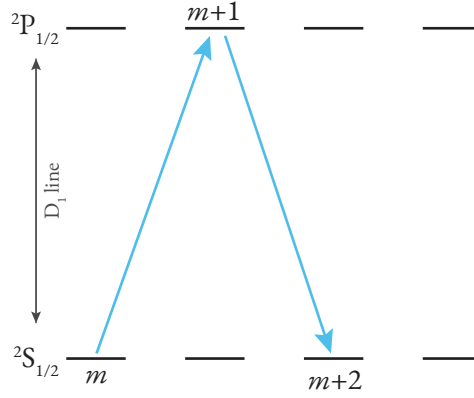


Figure 3.10.: Λ -system used in gray molasses cooling: It consists of two manifolds with equal J , connecting the two magnetic sublevels m and $m + 2$ in the ground state via $m + 1$ in the excited state.

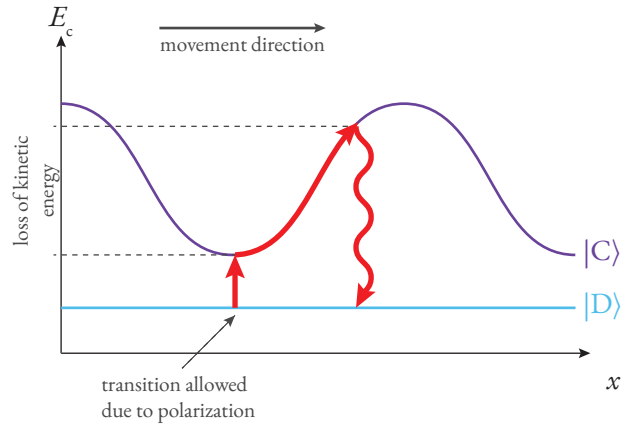


Figure 3.11.: Polarization-gradient in the gray molasses scheme: Atoms move along the light field and see different energy shifts E_c depending on their position. At positions with low light shift, the polarization allows that they transition from the dark state $|D\rangle$ to the coupling state $|C\rangle$ and move further in the light field losing kinetic energy until they decay back.

3. The 3-dimensional Magneto-optical Trap

ples to the light field via the excited state and experiences an energy shift $E_C \propto \frac{\Omega_{\text{eff}}^2}{\delta}$. The other, $|D\rangle$, is a dark state [21, 22].

The absence of coupling between these two states only persists as long as the atoms' kinetic energy is not considered. For atoms with momentum p , there is a non-zero transition probability $P \propto \left| \frac{p}{E_C} \right|^2$ [21]. This means that faster atoms are more prone to transition from the dark state to the coupling state, and that this transition is most likely in areas with low light shift.

The cooling effect in this scheme can now be understood as follows: Atoms move along the gray molasses light field with a velocity $v > 0$. At points with low light shift due to the polarization gradient, they are likely to transition from the dark state $|D\rangle$ to the coupling state $|C\rangle$. Moving further in the polarization-gradient field, their light shift energy E_C increases, at the cost of their kinetic energy. When they spontaneously decay back into the dark state $|D\rangle$ they lose an amount of energy on the order of the light shift E_C . This is illustrated in figure 3.11. The gray molasses light needs to be blue detuned ($\delta > 0$) because then the light shift is positive, and the atoms lose energy when falling back into the dark state $|D\rangle$. With this scheme, temperatures even below the recoil limit T_{recoil} can be reached [21, 22].

Gray Molasses with Lithium The D_1 line of lithium is just 10 GHz off the D_2 line. This avoids the need for separate laser system in a different wavelength regime and enables reusing optics of the magneto-optical trap for the gray molasses. Similar to the magneto-optical trap, a cooler and a repumper are needed: the former is blue detuned with respect to the $|^2S_{1/2}, F = 3/2\rangle \rightarrow |^2P_{1/2}, F = 3/2\rangle$ transition, the latter is blue detuned with respect to the $|^2S_{1/2}, F = 1/2\rangle \rightarrow |^2P_{1/2}, F = 3/2\rangle$. In contrast to cooling on the D_2 line, the excited manifold of the D_1 line is resolved, meaning the splitting between its excited state's hyperfine levels is larger than the line width [22].

Burchianti et al. implemented gray molasses for fermionic lithium in 2014. Their parameters were taken as a reference starting point for configuring the gray molasses of the FermiQP demonstrator setup [17]:

- laser intensities: $s_{0,\text{cooler}} = 2.7, \frac{s_{0,\text{repumper}}}{s_{0,\text{cooler}}} \approx 0.2$
- detunings: $\delta_{\text{cooler}} = +5.4\Gamma$, varying δ_{repumper} between $(\delta_{\text{cooler}} - 2\Gamma)$ and $(\delta_{\text{cooler}} + 3\Gamma)$

with $I_s = 7.59 \frac{\text{mW}}{\text{cm}^2}$ and $\Gamma = 5.8724 \text{ MHz}$ for the D_1 line [15].

In the following two sections, the laser setup for and the projected implementation of the 3-dimensional magneto-optical trap and the gray molasses in the FermiQP demonstrator will be described.

3.2. Preparation of the Trap Laser Light

In the FermiQP demonstrator, the cooling laser light for the 2-dimensional and the 3-dimensional magneto-optical traps as well as for the gray molasses is jointly produced on an optics board from where they are transferred to the experiment chamber via optical fibers.

The laser beams originate from two laser sources, one for D_2 light for the magneto-optical traps and one for D_1 light for the gray molasses. All beams produced by the setup consist of cooler and repumper light, which is separated by about 228 MHz, the hyperfine splitting of the $^2S_{1/2}$ ground state. For the 2-dimensional magneto-optical trap, the frequencies of the cooler and repumper light as well as their powers are fixed, for the 3-dimensional trap and the gray molasses light they need to be variable over an experiment cycle in order to compress and optimize the traps dynamically. The light for the 3-dimensional magneto-optical trap and the gray molasses is prepared on the same optical path, which is possible as both cooling schemes are carried out at the same position and which allows reusing the optics components. All beams need to have sufficient power levels such that several saturation intensities on the respective trap cross-sections are in reach for the 30 mm beam of the 2-dimensional trap ($10s_{0,D_2} \triangleq 180 \text{ mW}$) and the 7 mm beams for the 3-dimensional trap ($10s_{0,D_2} \triangleq 39 \text{ mW}$) and for the gray molasses cooling ($10s_{0,D_1} \triangleq 117 \text{ mW}$).

Laser sources

The 671 nm laser light for the D_2 and D_1 lines is produced for all aforementioned cooling beams by two Raman fiber amplifiers (MPB VRFA-P-1500-671-SF-PLUS, *Socrates* and *Plato*) with a specified output power of 1.5 W each. They are supplied with seed light by two single-mode diode lasers at 1342 nm (Toptica MDL pro, *Heraklitus* seeding *Socrates*, and *Zeno* seeding *Plato*), delivering around 20 mW of power. Each fiber amplifier contains a frequency-doubling stage creating a 671 nm laser beam of 1 mm diameter from the amplified 1342 nm light. The seed lasers are offset-locked to a global reference laser that itself is locked to an ultra-low expansion cavity. The offset locking allows shifting the laser frequencies of the D_2 and the D_1 light arbitrarily by up to 10 GHz. The interplay of these lasers is outlined in figure 3.12.

The main advantage of using the Raman fiber amplifiers is that they produce enough optical power to simultaneously supply all three aforementioned traps with light. An alternative would be separate laser sources, each of which would need to be frequency-locked and monitored independently. During the writing of the thesis, the Raman fiber amplifiers showed signs of substantial degradation as their output power decreased by over 20 % in only a few weeks of intermittent operation. The details and the severity of this degradation are presented in [23]. As the experimenters of FermiQP as well as the manufacturer of the amplifier could not come up with a quick and reliable solution to this problem that could be verified during the writing of this thesis, it stays uncertain whether the Raman fiber amplifiers can be used long-term for the laser cooling within the FermiQP demonstrator. An alternative approach would be amplification of the seed light using tapered amplifier chips.

3. The 3-dimensional Magneto-optical Trap

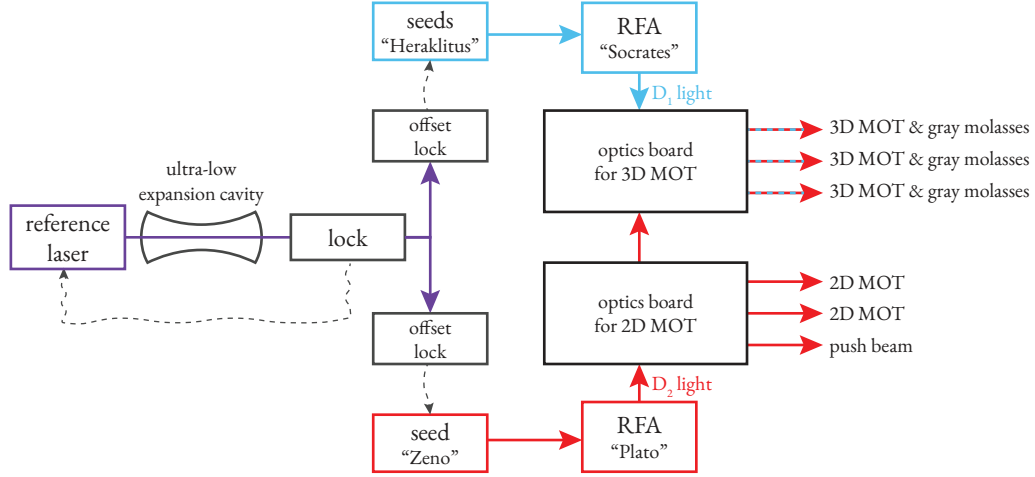


Figure 3.12.: Schematic of the cooling laser setup: Two Raman fiber amplifiers (RFA) provide light for the optics setups that prepare the light used in the magneto-optical traps and the gray molasses. This light is offset-locked via the amplifiers' seeds to a global reference laser which, in turn, is locked to a reference cavity.

Important Optical Elements

The following optical components were among the main building blocks of the part of the optics setup built within the scope of this thesis, which is described further below:

- **Polarizing beam splitter cube:** Polarizing beam splitter (PBS) cubes spatially split a laser beam into its $|H\rangle$ - and $|V\rangle$ -polarized components. The $|H\rangle$ component passes through the cube while the $|V\rangle$ component is deflected. In the setup described below, polarizing beam splitter cubes are used for splitting a laser beam into portions of arbitrary power using a preceding half-wave plate for setting the incident polarization accordingly, and for overlapping two beams of different polarization into a common spatial mode. The polarizing beam splitter cubes used for building the laser setup were manufactured by CeNing optics with a specified transmission extinction ratio error of $\frac{1}{1000}$ and a surface reflectivity of $< 0.25\%$.
- **Wave plate:** Wave plates allow changing the polarization of a beam. They are made of birefringent crystals cut to the right length such that there is a defined phase retardation between the fast and the slow axis of the crystal. Half-wave plates generate a 180° phase difference, quarter-wave plates generate a 90° phase difference between their axes. Depending on the angle between the axes of the crystal and the polarization components of the beam, half-wave plates can turn linear polarization into any other arbitrary linear polarization, whereas quarter-wave plates introduce ellipticity in the polarization and hence can generate circularly polarized light. Using a quarter- and a half-wave plate, linear polarization can be turned into any arbitrary polarization state. For turning an arbitrary polarization state into any other polarization state, an arrangement of quarter-, half-, and another quarter-wave plate is necessary as a single quarter-wave

3. The 3-dimensional Magneto-optical Trap

plate cannot arbitrarily change the ellipticity of incident elliptical light.² The wave plates used for building the laser setup were zero-order wave plates sold by Laser Components (part numbers: WPZ-671-04-2-R05, WPZ-671-09-2-R10, WPZ-671-04-4-R05, WPZ-671-09-4-R10) with a specified retardance threshold of $\frac{\lambda}{300}$ and reflectance of $< 0.2\%$.

- **Acousto-optic modulator:** Acousto-optic modulators (AOM) allow changing the optical frequency of a laser beam by multiples of the operating frequency f_{AOM} , typically in the order of 1×10^2 MHz. The beam is sent through a crystal in which the index of refraction n is spatially modulated perpendicular to the beam direction by an acoustic wave of frequency f_{AOM} . The incident laser light is diffracted on this spatial modulation of the index of refraction, leading to multiple light beams after of the modulator at angles η_m with $\sin \eta_m = m \frac{\lambda_{\text{light}}}{\lambda_{\text{acoustic}}}$ where $m \in \{\dots, -2, -1, 0, 1, 2, \dots\}$ is the order of each refracted beam and $\lambda_{\text{light}}, \lambda_{\text{acoustic}}$ are the optical and acoustic wave lengths. A beam of order m is frequency-shifted by $\Delta f = m f_{\text{AOM}}$ [24]. In the optical setup described below, acousto-optic modulators are used for increasing or decreasing the frequency of a laser beam and as fast optical shutters by switching the diffraction on and off. Sending light forwards and backwards through an acousto-optic modulator using a mirror, a so-called double pass, doubles the frequency shift of the light and avoids the angular diffraction, which cancels out for both passes through the modulator. While propagating through the double pass, the light is polarization-turned from $|H\rangle$ to $|V\rangle$ using a quarter-wave plate that the laser beam traverses in forward and backward direction such that incoming and outgoing light can be separated on a polarizing beam splitter. Typical coupling efficiencies for the first order are 80 % to 90 %. The acousto-optic modulators used for building the laser setup were produced by Gooch & Housego (part numbers: 3080-120, frequency range: (80 ± 10) MHz, active aperture of 1 mm and 3110-120, frequency range: (110 ± 12) MHz, active aperture of 0.6 mm).
- **Telescope:** A telescope reduces the diameter of a collimated laser beam. It consists of two lenses, the first being convex ($f > 0$) focusing down the laser beam, the second being concave ($f < 0$) re-collimating the beam.
- **Incoupler:** An incoupler arrangement feeds a free-space laser beam into an optical fiber. The beam is focused down onto the tip of the fiber using an aspheric lens with an appropriate focal length such that the waist of the focused beam matches with the fiber size. Typical coupling efficiencies range between 80 % to 90 %.
- **Mirror:** In the setup described below, mirrors with a broadband anti-reflection coating for incidence angles from 0° to 45° from the vendors Thorlabs (part numbers: with a specified reflectivity of % at 0° and % at 45°) and Laser Components (part numbers: with a specified reflectivity of % at 0° and % at 45° , back-polished) were used. For the Laser Components mirrors, it was experimentally verified that arbitrary incident polarization states were transformed in the same way by different mirrors from the same batch at 45° incidence angle.

add part numbers and specs

²An intuitive example of why only a quarter- and a half-wave plate are not sufficient for turning an arbitrary polarization state into any other polarization state is the transformation of circular light into elliptical light of any arbitrary ellipticity: A quarter-wave plate always transforms circularly polarized light into linearly polarized light, so at least one additional quarter-wave plate is necessary for creating arbitrary ellipticity.

Outline of the Laser Setup

The necessary output beams for the traps and the gray molasses are created from the two input beams on the D_2 and the D_1 frequency as depicted in figure 3.13.

The D_2 light is offset-locked at -78 MHz below the actual D_2 transition frequency. It is split on a polarizing beam splitter into two paths for the 2-dimensional and the 3-dimensional magneto-optical trap (A in figure 3.13). The power splitting ratio was preliminarily planned as about $\frac{1}{3}$ for the 3-dimensional and $\frac{2}{3}$ for the 2-dimensional optical trap since the 2-dimensional trap needs to reach the required intensity for a larger trap cross-section, and it is the first cooling stage of the experiment bridging the large range from several hundred Kelvin to sub-Kelvin temperatures on two of three spatial axes.

2D Trap Branch The branch for the 2-dimensional trap can be blocked using a shutter and an acousto-optic modulator used as a fast optical switch steered by the experiment control system. The shutter is a loudspeaker magnet with a beam blocker attached to it and acts as an additional slow controllable beam blockade ensuring that definitely no light can pass. This acousto-optic modulator increases the laser frequency by $+78$ MHz such that the light is resonant with the D_2 transition again. Using another half-wave plate and beam splitter, a small fraction of the laser power is branched off for the push beam (B). This light is frequency-shifted by $+114$ MHz in order to be resonant with the cooler transition. The remaining light is used in the trap.

The experimenters consider adding an electro-optical modulator at this point for improving the trap. This modulator would add frequency sidebands at several MHz to the light. In the trap, these additional frequencies would address other velocity classes than the original light and might hence increase the loading rate of the trap.

After that the light is split in a power ratio of approximately 1:1 into cooler and repumper beams (C), each of which is fed through an acousto-optic modulator with driving frequencies of -114 MHz and $+114$ MHz for cooler and repumper respectively, which corresponds to the hyperfine splitting of the ground state manifold. When the magneto-optical traps are implemented, the frequency splitting between cooler and repumper might be experimentally optimized for maximizing fluorescence of the 2-dimensional and loading rate of the 3-dimensional magneto-optical trap. The two beams are then spatially overlapped on a beam splitter (D) and fed to two optical fibers leading to the experiment chamber (E).

3D Trap & Gray Molasses Branch From the branch of the D_2 light for the 3-dimensional trap, a small amount is branched off for offset-locking. The remaining light is sent through a modulator-shutter combination for programmatic beam blocking as explained above, here with a modulator frequency of -198 MHz. It is then spatially overlapped with the D_1 light (F). The D_1 light is also offset by $+78$ MHz, a part of it split off for offset locking, and fed through an identical programmatic beam blockade.

3. The 3-dimensional Magneto-optical Trap

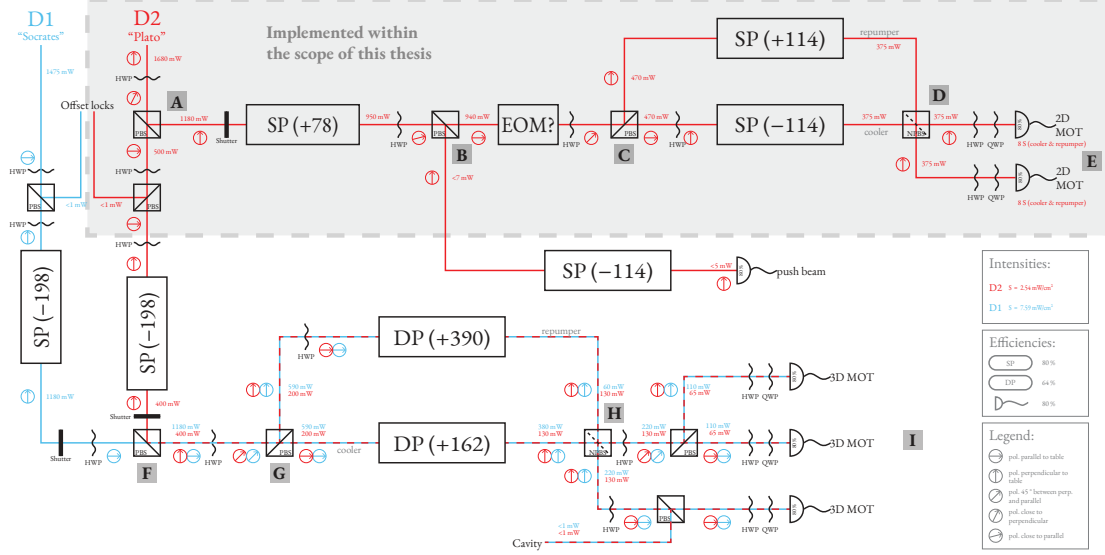


Figure 3.13.: Schematic of the laser setup for preparing the cooling light for the magneto-optical traps and the gray molasses: D₂ light is split into two branches for the 2-dimensional (to the right) and the 3-dimensional magneto-optical (to the bottom) traps at the first PBS (A). For the light for the 2-dimensional trap, a small amount of power is taken out for the push beam (B) before it is split into cooler and repumper light (C) and frequency-shifted by ± 114 MHz on acousto-optic modulators. It is then recombined (D) and split into two outputs (E). It is considered to add an electro-optical modulator (EOM) for improving the cooling effect of the light. This part of the laser setup was constructed within the scope of this thesis (gray box).

The light for the 3-dimensional trap and the D₁ light for the gray molasses are spatially overlapped (F), split into cooler and repumper (G) and frequency-shifted by 162 MHz and +390 MHz respectively on acousto-optic modulator double passes, recombined (H), and then split into three outputs (I).

Small amounts of power of both input laser beams are split off for locking on offset locks. A small amount of light for the 3-dimensional magneto-optical trap and the gray molasses is split off for monitoring the light frequencies on a cavity.

HWP and QWP stand for half- and quarter-wave plate respectively. The numbers in mW next to the beam lines are target powers assuming optically working laser sources.

3. The 3-dimensional Magneto-optical Trap

The combined beam of D_2 and D_1 light is then also split into two paths for cooler and repumper in a ratio of approximately 1:1 (G). Here, however, the light is fed through acousto-optic modulator double-passes as described in [23]. As the net deflection is zero in double passes, it allows a programmatic change of the frequency shift applied to each beam without the need to realign the beam path. Together with the ability to damp the laser power by reducing the modulators' radio-frequency driving power, frequency and power of each beam can be independently steered for compressing the 3-dimensional magneto-optical trap and for switching powers when applying the gray molasses. The cooler beam is frequency-shifted by about +162 MHz, the repumper by about +390 MHz, with the double-passes allowing for an adjustment range of several tens of MHz. The total frequency shift considering the initial offset, the blockade modulators and modulator amounts to $-78 \text{ MHz} - 198 \text{ MHz} + 390 \text{ MHz} = +114 \text{ MHz}$ in the cooler path and $-78 \text{ MHz} - 198 \text{ MHz} + 162 \text{ MHz} = -114 \text{ MHz}$ in the repumper path, which is again the hyperfine splitting of the ground state manifold. The light is then recombined (H) and split into three output beams (I) sent to the experiment chamber via optical fibers.

Implementation of the Laser Setup for the 2-dimensional Magneto-optical Trap

Within this thesis, the part of the laser setup providing the light for the 2-dimensional magneto-optical trap, as highlighted in figure 3.13, was built. Figure 3.14 shows a photograph of the implementation of this part of the setup. The light is prepared on the optics board in the following steps (letters reference points in figure 3.14):

- a The D_2 light is coming from the doubling stage of the Raman fiber amplifier "Plato" where the amplified 1342 nm light is frequency-doubled to 671 nm light. At this point, the laser beam has a $\frac{1}{e^2}$ diameter of about 1000 μm .
- b In order to prevent any inadvertent reflections travelling back into the amplifier, a Newport optical isolator (Newport ISO-04-650-MP-WP) was placed immediately after the doubling stage. In a power measurement, 30 dB damping (with the isolator inverted) and 95 % transmission could be attested in agreement with the specifications.
- c After the optical isolator, a quarter-wave plate is used to eliminate any elliptical polarization components from the beam caused by hitting mirrors with light that has polarization other than $|H\rangle$ and $|V\rangle$.
- d The D_2 light is split into the paths for the 2D and the 3D magneto-optical traps with a half-wave plate and a polarizing beam splitter. The splitting ratio between the beams was not yet fixed during the course of this thesis.
- e, f The light transmitted on the aforementioned beam splitter is again split and coupled into optical fibers leading to the offset lock (f) and to the other optics board hosting the rest of the setup (e, for details see [23]). The light reflected off on the beam splitter (d) is used for the push beam and the 2-dimensional magneto-optical trap.

3. The 3-dimensional Magneto-optical Trap

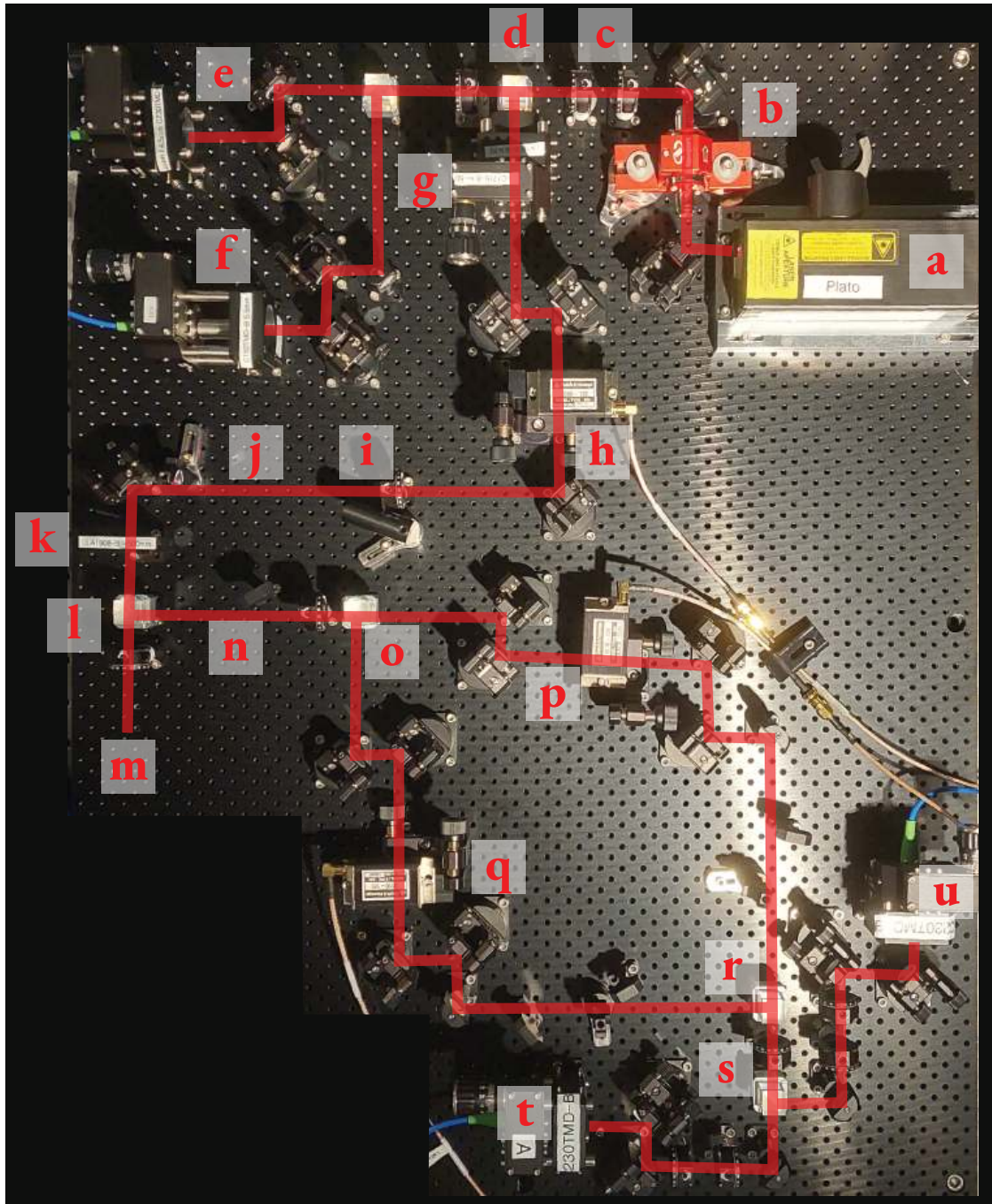


Figure 3.14.: Photograph of the part of the optics setup providing light for the 2-dimensional magneto-optical trap. The beam path and reference points have been added for orientation.

3. The 3-dimensional Magneto-optical Trap

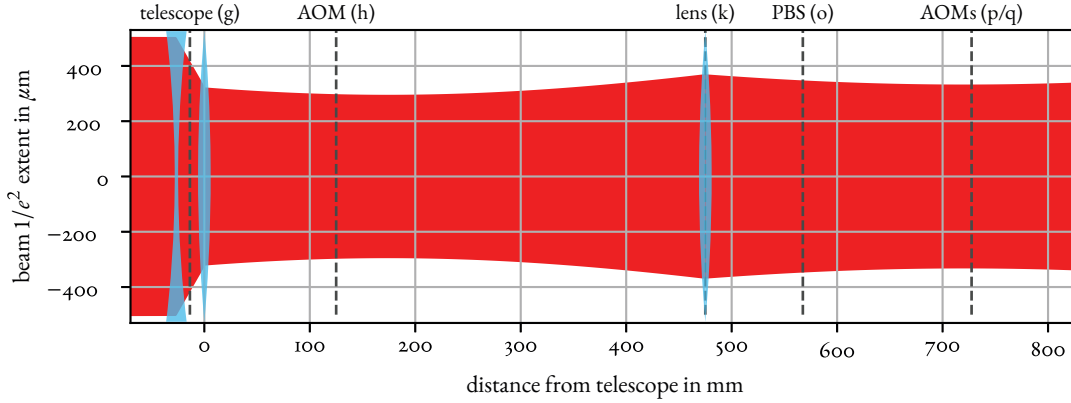


Figure 3.15.: Evolution of the beam shape along the beam path: The telescope (g) shrinks the beam from a diameter of $1000\ \mu\text{m}$ to about $600\ \mu\text{m}$ at the first acousto-optic modulator (h, 125 mm from the telescope). On the lens (k), the beam is focused again such that at the cooler and repumper acousto-optic modulators (p and q, about 730 mm from the telescope), the beam has a diameter of about $660\ \mu\text{m}$.

g As the acousto-optic modulators used in the setup require smaller beam diameters than the $1000\ \mu\text{m}$ beam supplied by the Raman fiber amplifier, a telescope for decreasing the beam diameter was placed after the aforementioned beam splitter cube. The telescope consists of a convex lens ($f = 75\ \text{mm}$) focusing the beam and a concave lens ($f = -50\ \text{mm}$) re-collimating it after about 30 mm. This reduces the beam diameter to about $650\ \mu\text{m}$ immediately after the second lens, the beam waist is now about $2w_0 = 600\ \mu\text{m}$ located about 175 mm away from the telescope. Lowering the beam diameter is a trade-off between a slimmer beam waist w_0 making the beam fitting better into the acousto-optic modulators' apertures and a larger beam divergence $\frac{\lambda}{\pi w_0}$ that would lead to even larger beam diameters after some propagation distance. The scaled-down beam reaches a diameter of about $700\ \mu\text{m}$ after about 475 mm after the telescope. In order to scale it down for the rest of the beam path on the board, an additional convex lens ($f = 500\ \text{mm}$) was placed in the beam path (k). In this way, the beam diameter is kept under $700\ \mu\text{m}$ on the remaining beam path with the waist (diameter $2w_0 \approx 650\ \mu\text{m}$) at a total distance of 720 mm from the telescope. These parameters were estimated based on a simulation in the software *GaussianBeam* [25], shown in figure 3.15.

h The slimmed-down light is then coupled through the first acousto-optic modulator operated at +78 MHz. The zeroth order of the outgoing beam is blocked at i. The first-order power efficiency of this acousto-optic modulator single pass is 83 % (see also table 3.1a). Thanks to the telescope, the beam diameter at this point is significantly smaller than the specified aperture.

i A half-wave plate sets the splitting ratio between light for the push beam (m) and light for the 2-dimensional magneto-optical trap.

j At this position the shutter will be placed in order to be able to completely bar any light from

3. *The 3-dimensional Magneto-optical Trap*

entering the magneto-optical trap.

- k Here the light is refocused using an $f = 500$ mm lens as described in point g. This sizes down the beam diameter such that it doesn't exceed the aperture of the acousto-optic modulators for creating the cooler and repumper beams (p, q).
- l The light is split into a few mW for the push beam (m) and the rest for the 2-dimensional magneto-optical trap.
- m Here the push beam light will be prepared using a single pass acousto-optic modulator driven at +114 MHz which serves as a frequency shifter and as a shutter.
- n At this point, space is left free for an electro-optical modulator that would add sidebands onto the light allowing for addressing more velocity classes in the trap and thus potentially increasing its loading rate.
- o With a half-wave plate and a polarizing beam splitter, the light is split into cooler (q) and repumper (p) paths. The polarizations of the beams are $|V\rangle$ of the cooler and $|H\rangle$ of the repumper beam.
- p, q The cooler (q) and repumper (p) paths each contain an acousto-optic modulator operated at -114 MHz and +114 MHz respectively. Thanks to the refocusing lens (k), the beam diameter approximately matches the modulators' apertures. The coupling efficiency is 76 % for the cooler and 81 % for the repumper (see also table 3.1a).
- r, s The cooler and repumper beam are spatially overlapped and split into two paths on a combination of two polarizing beam splitter cubes and a half-wave plate. Due to their polarizations, the cooler is reflected on the first cube (r) while the repumper passes through it, both leaving the cube on the same port. A half-wave plate then turns their respective polarizations to diagonal $|D\rangle$ and anti-diagonal $|A\rangle$. A subsequent polarizing beam splitter cube (s) splits both cooler and repumper into two equally strong, spatially overlapped beams.
- t, u The two resulting beams, both containing cooler and repumper frequencies, are coupled into fibers guiding the light to the experiment chamber. In each beam, a pair of a quarter- and half-wave plate allow for arbitrary corrections of the polarization if necessary. The coupling efficiencies after the assembly of the optics board are 84 % for fiber A (t) and 74 % for fiber B (u) for both cooler and repumper (see also table 3.1a). When the magneto-optical traps are implemented and the frequencies of the cooler and repumper beams are optimized, the light needs to be coupled into the two fibers from anew as the deflection angles on the respective acousto-optic modulators will also change.

Table 3.1 lists measured remaining power levels after each dissipating element (tab. 3.1a) as well as measured recombination (tab. 3.1b) and splitting ratios (tab. 3.1c).

3. The 3-dimensional Magneto-optical Trap

element		markers (fig. 3.14)	power after element
isolator		b	97 %
telescope		g	99 %
switching AOM	all orders	h	100 %
	positive orders	h - k	89 %
	first order	h - o	83 %
cooler AOM	all orders	q	97 %
	first order	q - r	76 %
repumper AOM	all orders	p	99 %
	first order	p - r	81 %
fiber A	cooler & repumper	s - t	84 %
	cooler	q - t	78 %
	repumper	p - t	81 %
fiber B	cooler & repumper	s - u	74 %
	cooler	q - u	71 %
	repumper	p - u	77 %

(a) Measured remaining powers after dissipating elements

beam	markers (fig. 3.14)	percentage
cooler	q - r	51 %
repumper	p - r	47 %

(b) Measured power ratios of the recombined cooler and repumper beams on the polarizing beam splitter cube r

beam	branch	markers (fig. 3.14)	ratio
cooler & repumper	A	s - t	50 %
	B	s - u	51 %
cooler	A	q - t	49 %
	B	q - u	53 %
repumper	A	p - t	51 %
	B	p - u	49 %

(c) Measured power splitting ratios into branches A and B on the polarizing beam splitter cube s

Table 3.1.: Measured power dissipations and power ratios on the optics board for the 2-dimensional magneto-optical trap

3. The 3-dimensional Magneto-optical Trap

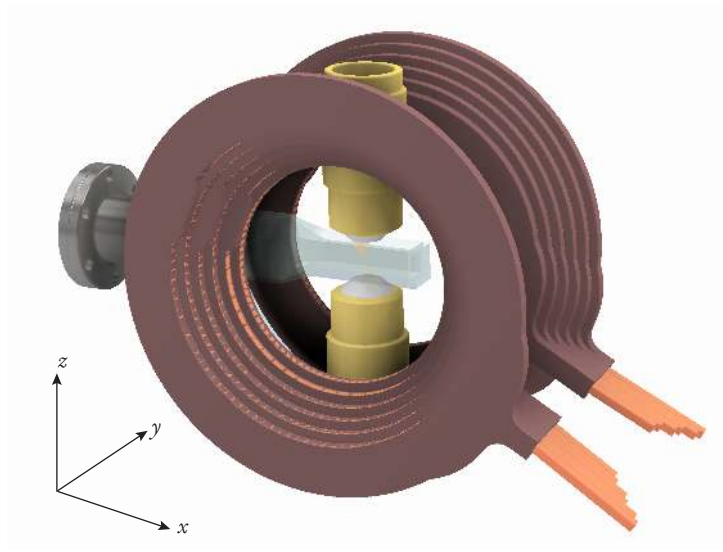


Figure 3.16.: Position of the glass cell between the microscope objectives and the Feshbach coils. The tightly packed vicinity of the glass cell determines the geometry of the magneto-optical trap.

3.3. Projected Implementation

In this section, the projected implementation of the 3-dimensional magneto-optical trap is presented. The intended geometry of the trap setup serves as a starting point for elaborating the arrangement and configuration of the optical setup around the glass cell for the trapping beams. The planned magnitude of magnetic gradients is shortly mentioned. The section concludes with a forecast about key properties of the trap.

Geometry

The 3-dimensional magneto-optical trap of the FermiQP demonstrator is loaded from the atomic beam originating from the 2-dimensional magneto-optical trap. It is guided through a differential pumping stage separating the high and the ultra-high vacuum regions of the experiment chamber. The trap is located in the front part of the glass cell. The space around the glass cell is tightly packed with the two microscope objectives sitting above and below the trap and the Feshbach coils placed left and right of the incoming atomic beam, as shown in figure 3.16. As a reminder, the reference coordinate system of the experiment chamber is that x is along the atomic beam, y is to the left as seen in the direction of the atomic beam, and z is in upward direction.

The magneto-optical trap needs three pairs of beams, one for each spatial degree of freedom that the atoms should be cooled along. For each pair, a beam is shot in from one side and retroreflected after passing through the glass cell. Due to the tightly packed vicinity of the glass cell, the beam axes cannot match with the Cartesian coordinate axes: no beams can be shot along the z axis which is blocked by the

3. The 3-dimensional Magneto-optical Trap

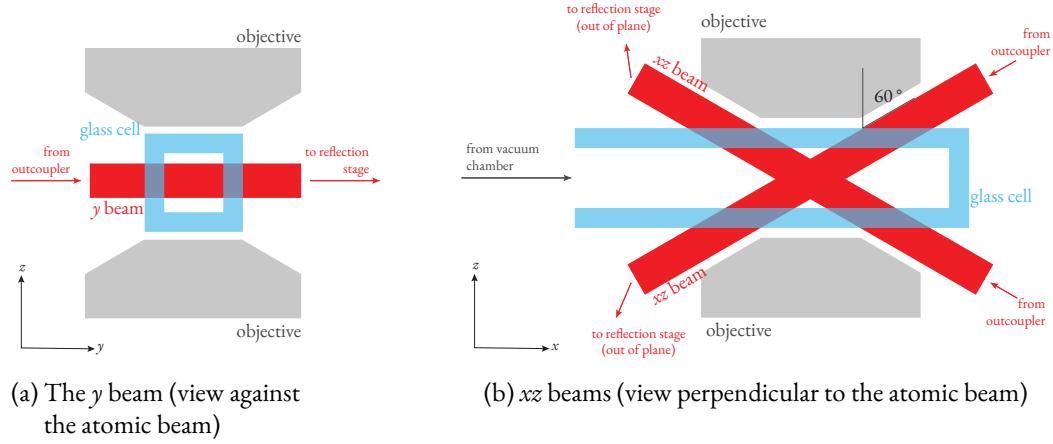


Figure 3.17.: Schematic side views of the glass cell and the trap beams: The y beam comes in from the left/right. The two xz beams come in under shallow angles, with incidence angles of 60° with respect to the glass cell surface normal. Behind the glass cell, the xz beams are deflected away to their respective reflection stages. The beams have a diameter of 7 mm. The glass cell has a side length of 20 mm and 4 mm-thick walls. Dimensions are to scale in this schematic. The change of the incidence angle of the xz beams within the glass due to refraction was neglected in this schematic.

objectives, and no beam can be shot directly along the atomic beam axis (x) because no retroreflection would be possible on the other side of the glass cell.

Instead, two beams are shone in in the xz plane where they fit through: The geometry of the microscope objectives only permits shooting beams into the glass cell at shallow angles, namely with an incidence angle of 60° with respect to the surface normal of the glass cell, as depicted in figure 3.17b. These beams provide cooling and confinement along the atomic beam axis (x , with an angle of $\theta = 30^\circ$ between light propagation \vec{k} and velocity \vec{v} of the atomic beam) and the up-down axis (y). The third beam is shot in along the y axis, i.e. from left to right (see figure 3.17a). The beams are reflected back on reflection stages a bit away from the glass cell.

Optics around the Experiment Chamber

The six cooling laser beams for the 3-dimensional magneto-optical trap are transferred from the optics board to the experiment chamber with optical fibers where they are outcoupled and prepared on outcoupling stages.

The y beam will be reflected back directly on a reflection stage at the other side of the glass cell. The two xz beams are shot into the glass cell from the upper and lower front of the glass cell through the upper surfaces at an incidence angle of 60° in order not to be blocked by the microscope objectives (as explained in the geometry section above, see figure 3.17). For reflecting these beams back into the glass cell, they are first guided away from the experiment chamber onto stand-alone reflection stages as

3. The 3-dimensional Magneto-optical Trap

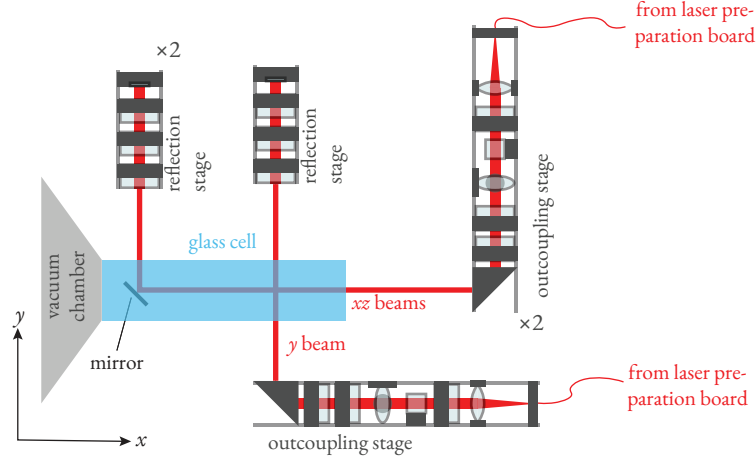


Figure 3.18.: Schematic of the optics for the 3-dimensional magneto-optical trap from above: The reflection stages of the xz beams would not fit between the glass cell and the vacuum chamber. Instead, the xz beams are reflected away from the chamber on a mirror onto the xz reflection stages away from the chamber.

there wouldn't be enough space for these stages between the vacuum chamber and the glass cell (see figure 3.18).

Outcoupling Stages The outcoupling stages consist of optical elements for collimating, polarization-cleaning, and polarization-preparing the light, mounted in an optical cage system. A schematic of the stages is shown in figure 3.19.

The light leaving the optical fiber has a divergence angle of $\theta_{\text{divergence}} = \frac{\lambda}{\pi w} = \frac{671 \text{ nm}}{\pi 2.25 \text{ } \mu\text{m}} = 95 \text{ mrad}$ set by the beam waist $w = 2.25 \text{ } \mu\text{m}$ at the fiber tip. In order to collimate it to a beam of $\frac{1}{e^2}$ diameter of 7 mm, hence radius of $r_{1/e^2} = 3.5 \text{ mm}$, a lens of focal length $f = \frac{r_{1/e^2}^2}{\tan \theta_{\text{divergence}}} = \frac{3.5 \text{ mm}}{95 \text{ mrad}} \approx 35 \text{ mm}$ [26] is installed in the outcoupling stage such that the fiber tip is in the focal point.

In order to get rid of non-linear polarization components that the light might have acquired while travelling in the fiber, it is cleaned using a combination of a half-wave plate and a polarizing beam splitter that it transmits through.

Then a beam sampler reflects out a small fraction of the light onto a photodiode for power monitoring. Note that the power is monitored after polarization cleaning in order to check the effective power that is available for trapping³.

Finally, the polarization of the trapping beam can be set using a quarter- and a half-wave plate.

³The power is not monitored on the other beam splitter port as then one could not distinguish between polarization-induced and supply-induced power changes. It is also not checked by monitoring the transmitted power on one of the system's back-polished mirrors as the absolute power transmitted through these mirrors would be too little.

3. The 3-dimensional Magneto-optical Trap

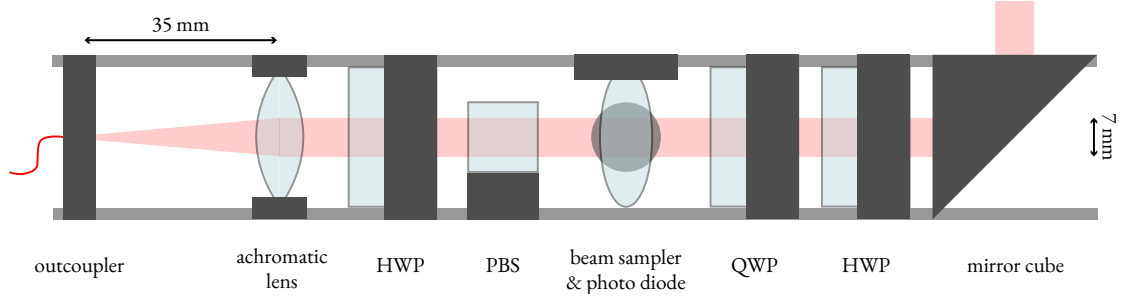


Figure 3.19.: Schematic of the outcoupling stages in an optical cage system: The trapping light coming from an optical fiber is collimated with an achromatic lens with a focal length of 35 mm such that the beam has a $\frac{1}{e^2}$ diameter of 7 mm. The polarization is cleaned using a half-wave plate and a polarizing beam splitter the light is transmitted through. With a beam sampler a small amount of light is reflected out of the axis and shot onto a photodiode for power monitoring. The clean linear light is then polarization-prepared on a quarter- and a half-wave plate and reflected out on a mirror cube.

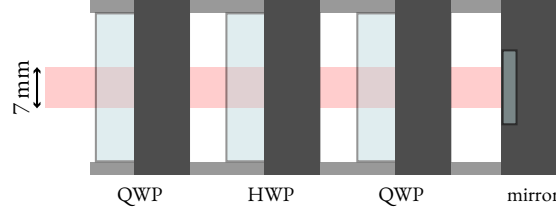


Figure 3.20.: Schematic of the reflection stage in an optical cage system: Incoming light is sent through a quarter-, a half-, and another quarter-wave plate, and then reflected on a mirror. It leaves the stage propagating through the three wave plates again in reverse order.

Reflection Stages The reflection stages consist of an cascade of a quarter-, a half-, and another quarter-wave plate and a mirror mounted in a cage system, as depicted in figure 3.20. This threefold wave plate combination is traversed by the light twice, forwards and backwards, and allows for arbitrary changes of polarization. Only using two wave plates in the reflection stage would not suffice as a combination of only one quarter- and one half-wave plate cannot map every polarization to any other arbitrary polarization, as pointed out in section 3.2.

Polarization

The trapping light needs to have circular polarization at the trap position in the glass cell, either with left or right helicity for both the forward and the backward pass, depending on the direction of the magnetic gradient, as explained in section 3.1. Since the polarization cannot be measured within the glass cell at the time of operation, the approximate configuration of the optics for attaining the necessary polarization was estimated beforehand.

3. The 3-dimensional Magneto-optical Trap

In the following, the Jones vector notation for polarization in the horizontal-vertical basis $\{|H\rangle, |V\rangle\}$ is going to be used to denote the circular polarization states $|R\rangle$ and $|L\rangle$ and the diagonal polarization states $|D\rangle$ and $|A\rangle$:

$$\text{circular:} \quad |R\rangle = \frac{1}{\sqrt{2}} (|H\rangle - i|V\rangle), \quad |L\rangle = \frac{1}{\sqrt{2}} (|H\rangle + i|V\rangle) \quad (3.20)$$

$$\text{diagonal:} \quad |D\rangle = \frac{1}{\sqrt{2}} (|H\rangle + |V\rangle), \quad |A\rangle = \frac{1}{\sqrt{2}} (|H\rangle - |V\rangle) \quad (3.21)$$

Here, horizontal polarization $|H\rangle$ is defined as parallel to the glass cell surface where the beam enters the cell, vertical polarization $|V\rangle$ is perpendicular to $|H\rangle$. For the y beams, $|V\rangle$ is also parallel to the glass cell surface. For the xz beams, $|V\rangle$ encloses a 30° angle with the surface normal of the glass cell surface.

For the y axis trap beam entering the glass cell from the left or right, the circular polarization can directly be set on the wave plates in the outcoupling stage. As the light enters the glass cell perpendicular to its surface, the polarization will not be affected when transmitted through the glass.

For the two xz beams entering at shallow angles with $\xi = 60^\circ$ between the surface normal and the beam, the difference in transmission coefficients for $|H\rangle$ and $|V\rangle$ polarization components needs to be considered and the wave plates on the outcoupling and the reflection stages must be set accordingly.

The glass cell is made of fused silica with a refractive index of $n = 1.456$ at 671 nm [27]. According to Snell's law, for the xz beams the angle between the light and the surface normal in the glass is $\xi_{\text{glass}} = \arcsin \frac{\sin \xi}{n} = 36.5^\circ$ [28]. The transmission coefficients for the two polarization components are then [28]

$$\begin{aligned} t_{|H\rangle, \text{air} \rightarrow \text{glass}}(\xi, \xi_{\text{glass}}) &= \frac{2 \cos \xi}{\cos \xi + n \cos \xi_{\text{glass}}} \\ t_{|H\rangle, \text{glass} \rightarrow \text{air}}(\xi, \xi_{\text{glass}}) &= \frac{2n \cos \xi_{\text{glass}}}{n \cos \xi_{\text{glass}} + \cos \xi} \\ t_{|V\rangle, \text{air} \rightarrow \text{glass}}(\xi, \xi_{\text{glass}}) &= \frac{2 \cos \xi}{n \cos \xi + \cos \xi_{\text{glass}}} \\ t_{|V\rangle, \text{glass} \rightarrow \text{air}}(\xi, \xi_{\text{glass}}) &= \frac{2n \cos \xi_{\text{glass}}}{\cos \xi_{\text{glass}} + \cos \xi} \end{aligned} \quad (3.22)$$

where the s and p components of the polarization have been mapped to the $|H\rangle$ and $|V\rangle$ basis vectors respectively. For the y beam, they evaluate to $t_{\text{air} \rightarrow \text{glass}}(0^\circ, 0^\circ) = 0.814$, $t_{\text{glass} \rightarrow \text{air}}(0^\circ, 0^\circ) = 1.186$.⁴ For the xz beams, they evaluate to $t_{|H\rangle, \text{air} \rightarrow \text{glass}}(\xi, \xi_{\text{glass}}) = t_{|H\rangle, \text{glass} \rightarrow \text{air}}(\xi, \xi_{\text{glass}}) = 0.916$, $t_{|V\rangle, \text{air} \rightarrow \text{glass}}(\xi, \xi_{\text{glass}}) = t_{|V\rangle, \text{glass} \rightarrow \text{air}}(\xi, \xi_{\text{glass}}) = 0.999$.

The total transmission coefficient through the 4 mm-thick wall of the glass consists of the transmission

⁴Note that it is not unphysical if $t > 1$. The transmitted power on a surface from air to a material with $n > 1$ is $\frac{n \cos \xi_{\text{transmitted}}}{\cos \xi_{\text{incident}}} t^2$ which is always less than 1 [28].

Check values and propagate if they were wrong

3. The 3-dimensional Magneto-optical Trap

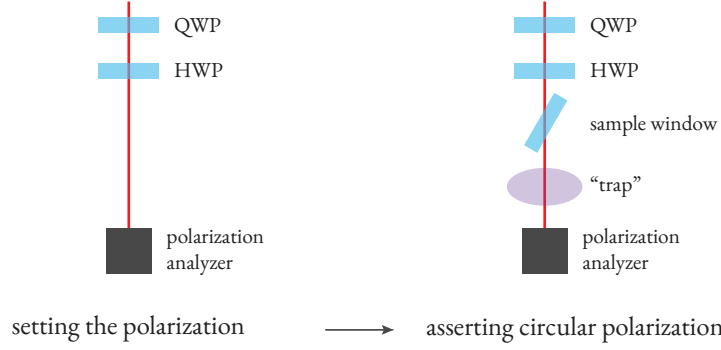


Figure 3.21.: Schematic of the experimental setup for verifying the polarization of the incident trapping light for the first pass through the glass cell: At first, the predicted polarizations (see equations 3.25) were set and verified using a polarization analyzer. Then a sample glass plate was put in and circular polarization after the plate (the “trap” position) was asserted with the polarization analyzer.

coefficients into glass and back into air:

$$t_y = t_{|H\rangle, \text{air} \rightarrow \text{glass}}(0^\circ, 0^\circ) \cdot t_{|H\rangle, \text{glass} \rightarrow \text{air}}(0^\circ, 0^\circ) = 0.965 \quad (3.23)$$

$$t_{xz, |H\rangle} = t_{|H\rangle, \text{air} \rightarrow \text{glass}}(\xi, \xi_{\text{glass}}) \cdot t_{|H\rangle, \text{glass} \rightarrow \text{air}}(\xi, \xi_{\text{glass}}) = 0.839 \quad (3.24)$$

$$t_{xz, |V\rangle} = t_{|V\rangle, \text{air} \rightarrow \text{glass}}(\xi, \xi_{\text{glass}}) \cdot t_{|V\rangle, \text{glass} \rightarrow \text{air}}(\xi, \xi_{\text{glass}}) = 0.998$$

First pass In order to attain circular polarization on the first pass through the glass cell, these polarization-dependent losses need to be pre-compensated when choosing the polarization before the glass cell surface:

$$\left| \psi_{\text{before cell, right left}} \right\rangle = \frac{1}{\sqrt{\frac{1}{t_{|H\rangle}^2} + \frac{1}{t_{|V\rangle}^2}}} \left(\frac{|H\rangle}{t_{|H\rangle}} \mp i \frac{|V\rangle}{t_{|V\rangle}} \right) = 0.765 |H\rangle \mp 0.644i |V\rangle \quad (3.25)$$

For verifying these polarizations in a mock setup, a sample fused silica glass plate of thickness 4.04 mm was placed at an angle of 60° with respect to a 671 nm laser beam. This glass plate acts as the surface through which the light enters the glass cell. Using a quarter- and a half-wave plate, the polarization before the plate could be arbitrarily set by monitoring it on a polarization analyzer (Thorlabs PAX 1000IR). Then the glass plate was put into the beam path and circular polarization was asserted after the glass plate, as outlined in figure 3.21. The results are displayed in table 3.2 and show that the aforementioned estimated polarizations are a good estimate for producing circular polarization in the glass cell.

Second pass In order to attain the same circular polarization on the second pass through the glass cell, the wave plates on the reflection stages must be set accordingly. Their required configuration

3. The 3-dimensional Magneto-optical Trap

target polarization	set before glass plate	measured after glass plate
$ R\rangle$	$0.78 H\rangle + (-0.02 - 0.63i) V\rangle$	$0.70 H\rangle + (0.00 - 0.71i) V\rangle$
$ L\rangle$	$0.75 H\rangle + (-0.01 + 0.67i) V\rangle$	$0.70 H\rangle + (0.00 + 0.71i) V\rangle$

Table 3.2.: Results of the experimental verification of the preset polarization for the first pass through the glass cell, as outlined in figure 3.21. The measured polarizations after the glass plate confirm that the proposed pre-compensation (3.25) is a good estimate. All values are outputs of a polarization analyzer (Thorlabs PAX 1000IR), transformed from the azimuth-ellipticity basis to the Jones basis as described in the appendix chapter A.

is determined experimentally since the glass surfaces and mirrors in the beam path introduce many polarization changes that are hard to deduct from principle. Again, a mock setup with a sample glass plate at an angle of 60° with respect to the beam is used. This time, it acts as the surface which the light leaves and then re-enters the glass cell through.

In the mock setup, light is transmitted through a polarizing beam splitter cube and then circularly polarized using a quarter-wave plate. This light mimics the trap light before leaving the glass cell on the first pass. It is then transmitted through the sample glass plate at the shallow angle of 60° , simulating the exit from the glass cell. Afterwards the light is deflected onto a mock reflection stage, made up of a quarter-, a half-, and another quarter-wave plate, and finally onto a mirror sending the light back through the setup such that it reaches the beam splitter cube again. This arrangement is outlined in figure 3.22. For the mirrors used for deflecting the beam onto the reflection stage (Laser Componentets), it was verified that individual mirrors all change the polarization in the same way at an incidence angle of 45° .

model
name

The ideal wave plate configuration on the reflection stage is now identified by monitoring the power reflected on the polarizing beam splitter depending on the wave plate configuration: Light passing back through the setup with the same circular polarization as on the first pass will be completely transmitted back through the beam splitter cube after traversing the quarter-wave plate in reverse direction. This means that for the desired configuration, all light of the second pass will be transmitted on the beam splitter cube, and the deflected power on the cube is minimal.

The complete evolution of polarization in the setup for right polarization in the cell is

$$\begin{array}{ccccccccccc} \longrightarrow & |H\rangle & \longrightarrow & |R\rangle & \longrightarrow & |\psi_R\rangle & \longrightarrow & M|\psi_R\rangle & \longrightarrow & |R\rangle & \longrightarrow & |H\rangle & \longrightarrow & (3.26) \\ \text{beam} & & \text{quarter} & & \text{mirror \&} & \text{mirror} & & \text{wave plates \&} & & \text{quarter} & & \text{beam splitter} & & \\ \text{splitter} & & \text{wave plate} & & \text{wave plates} & & & \text{mirror} & & \text{wave plate} & & \text{port 1} & & \end{array}$$

and for left polarization in the cell it is analogously

$$\begin{array}{ccccccccccc} \longrightarrow & |H\rangle & \longrightarrow & |L\rangle & \longrightarrow & |\psi_L\rangle & \longrightarrow & M|\psi_L\rangle & \longrightarrow & |L\rangle & \longrightarrow & |H\rangle & \longrightarrow & (3.27) \\ \text{beam} & & \text{quarter} & & \text{mirror \&} & \text{mirror} & & \text{wave plates \&} & & \text{quarter} & & \text{beam splitter} & & \\ \text{splitter} & & \text{wave plate} & & \text{wave plates} & & & \text{mirror} & & \text{wave plate} & & \text{port 1} & & \end{array}$$

with the polarization flip $M = \begin{pmatrix} 1 & 0 \\ 0 & -1 \end{pmatrix}$ caused by a mirror at 0° . The polarizations $|\psi_R\rangle$ and $|\psi_L\rangle$ identify the ideal wave plate configuration and are hence the observed parameter looked for in the

3. The 3-dimensional Magneto-optical Trap

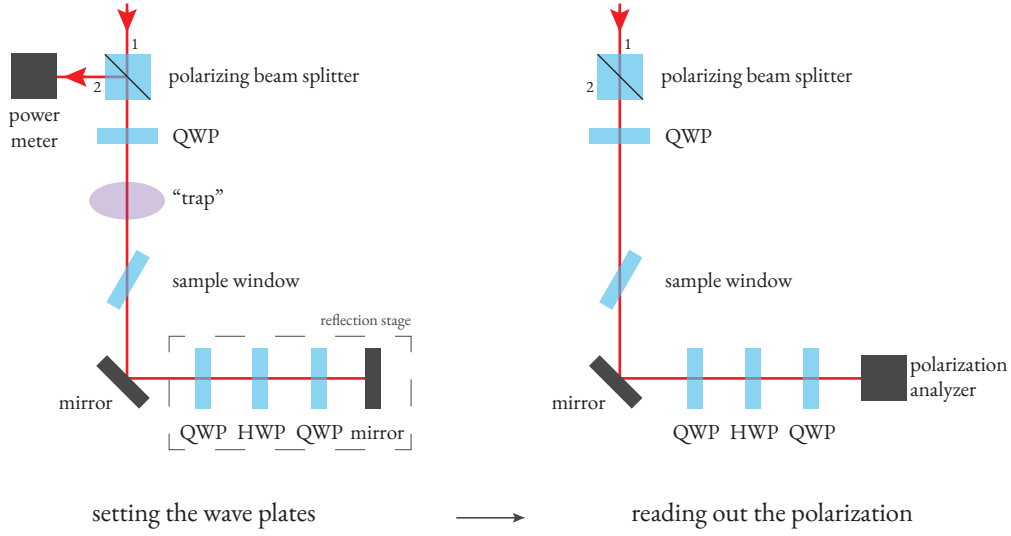


Figure 3.22.: Schematic of the experimental setup for finding the right configuration of the wave plates on the reflection stages: In a first step, the wave plate configuration on the “reflection stage” is optimized for circular polarization in the “trap” by minimizing the output power on port 2 of the beam splitter cube. Then the polarization after the forward pass through the reflection stage, which identifies the optimal wave plate configuration, is measured using a polarization analyzer.

mock setup. $|\psi_R\rangle$ and $|\psi_L\rangle$ can be measured by replacing the mirror with the polarization analyzer after an optical wave plate configuration has been found, as outlined in figure 3.22.

The ideal polarizations were identified by finding the minima of light power on port 2 of the beam splitter ($< 1\%$ of the power after the sample window). They are listed in table 3.3.

When building the trap, the polarization presets for the first and the second pass through the glass cell (tables 3.2 and 3.3) should be deemed an initialization point for getting a first signal. The trap then needs to be optimized by varying the polarization configuration and monitoring its loading rate with fluorescence imaging.

target polarization P	polarization $ \psi_P\rangle$ in reflection stage
$ R\rangle$	$0.71 H\rangle + (0.70 + 0.09i) V\rangle$
$ L\rangle$	$0.62 H\rangle + (0.77 + 0.17i) V\rangle$

Table 3.3.: Experimentally found ideal polarizations after the first pass through the reflection stage. For these polarizations, the light is circularly polarized on the backward pass through the mock setup (see figure 3.22). All values are outputs of a polarization analyzer (Thorlabs PAX 1000IR), transformed from the azimuth-ellipticity basis to the Jones basis as described in the appendix chapter A.

3. The 3-dimensional Magneto-optical Trap

Intensity

The intensity of the trapping light is reduced along the optical path by the reflections on the glass surfaces and scattering by the atoms in the trap. In the following, $T_{1 \rightarrow 2}(\xi_1, \xi_2) = \frac{n_2 \cos \xi_2}{n_1 \cos \xi_1} t_{1 \rightarrow 2}^2$ quantifies the power transmitted on a surface from medium 1 to medium 2 with beam angle ξ_i in medium i and a transmission coefficient of t [28].

In the first pass, the intensity loss is due to reflections on the outer and inner surface of the glass cell wall. For the y axis beam that hits the glass cell perpendicular to its surface, the remaining relative power is polarization-independent and determined by the transmission coefficient at 0° (equations 3.22). For the xz axis beams (with polarization state $0.765 |H\rangle \mp 0.644i |V\rangle$, cf. equation 3.25), the remaining relative power is composed of the transmissions at an incidence angle $\xi = 60^\circ$ for the two polarization components:

$$p_{y, \text{first pass}} = T_{y, \text{in}} = T_{\text{air} \rightarrow \text{glass}}(0^\circ) T_{\text{glass} \rightarrow \text{air}}(0^\circ) = \left(\frac{1}{n} t_{\text{air} \rightarrow \text{glass}}^2(0^\circ) \right) \left(n t_{\text{glass} \rightarrow \text{air}}^2(0^\circ) \right) = 0.932 \quad (3.28)$$

$$\begin{aligned} p_{xz, \text{first pass}} &= T_{xz, \text{in}} = 0.765^2 T_{xz, |H\rangle} + 0.644^2 T_{xz, |V\rangle} \\ &= 0.765^2 \left(\frac{1}{n} t_{|H\rangle, \text{air} \rightarrow \text{glass}}^2(\xi) \right) \left(n t_{|H\rangle, \text{glass} \rightarrow \text{air}}^2(\xi_{\text{glass}}) \right) \\ &\quad + 0.644^2 \left(\frac{1}{n} t_{|V\rangle, \text{air} \rightarrow \text{glass}}^2(\xi) \right) \left(n t_{|V\rangle, \text{glass} \rightarrow \text{air}}^2(\xi_{\text{glass}}) \right) \\ &= 0.765^2 \cdot (0.916^2 \cdot 0.999^2) + 0.644^2 \cdot (0.999^2 \cdot 0.916^2) = 0.837 \end{aligned} \quad (3.29)$$

These values could be asserted by measuring optical power in a mock setup using a sample glass plate, similar to the ones for setting the polarization (figures 3.21 and 3.22). The measured intensity losses are listed in table 3.4.

In the second pass, the first loss T_{out} is due to reflections on the two surfaces of the other glass cell wall upon exit from the glass cell. There, both beams have circular polarization before entering the glass:

$$T_{y, \text{out}} = T_{y, \text{in}} = 0.932 \quad (3.30)$$

$$T_{xz, \text{out}} = \frac{1}{2} T_{xz, |H\rangle} + \frac{1}{2} T_{xz, |V\rangle} = 0.837 \quad (3.31)$$

The second loss T_{in} is due to entering the glass cell again with the same polarization as in the first pass. In addition, relative losses $(1 - p_{\text{scatter}})$ from scattering on the atoms in the first pass affect the beam power in the second pass. The remaining power in the second pass compared to the power in the first pass is

$$p_{y, \text{first pass} \rightarrow \text{second pass}} = p_{\text{scatter}} \cdot T_{y, \text{out}} T_{y, \text{in}} = 0.867 p_{\text{scatter}} \quad (3.32)$$

$$p_{xz, \text{first pass} \rightarrow \text{second pass}} = p_{\text{scatter}} \cdot T_{xz, \text{out}} T_{xz, \text{in}} = 0.701 p_{\text{scatter}} \quad (3.33)$$

3. The 3-dimensional Magneto-optical Trap

	predicted loss	measured loss
$p_{y,\text{first pass}}$	93.2 %	94 %
$p_{xz,\text{first pass}}$	83.7 %	84 %
$p_{y,\text{first pass} \rightarrow \text{second pass}}$	$86.7 \% \cdot p_{\text{scatter}}$	
$p_{xz,\text{first pass} \rightarrow \text{second pass}}$	$70.1 \% \cdot p_{\text{scatter}}$	
$p_{y,\text{input} \rightarrow \text{second pass}}$	$81.0 \% \cdot p_{\text{scatter}}$	
$p_{xz,\text{input} \rightarrow \text{second pass}}$	$58.6 \% \cdot p_{\text{scatter}}$	

Table 3.4.: Remaining intensities on the first and the second pass through the glass cell surface for the y and the xz beams. First pass intensities were experimentally verified on a mock setup.

and the remaining power in the first pass compared to the original input power is

$$p_{y,\text{input} \rightarrow \text{second pass}} = T_{y,\text{in}} \cdot p_{\text{scatter}} \cdot T_{y,\text{out}} T_{y,\text{in}} = 0.810 p_{\text{scatter}} \quad (3.34)$$

$$p_{xz,\text{input} \rightarrow \text{second pass}} = T_{xz,\text{in}} \cdot p_{\text{scatter}} \cdot T_{xz,\text{out}} T_{xz,\text{in}} = 0.586 p_{\text{scatter}}. \quad (3.35)$$

p_{scatter} depends on the geometry and density of the trapped atom cloud as well as the scattering rate, which in turn depends on the laser parameters.

Table 3.4 lists all of these relative intensity losses.

In order to achieve a similar cooling effect in both directions for each axis, meaning the first and second pass through the glass cell, the beam diameters d could be reduced in the second pass with a focusing lens or by slightly displacing the achromatic lens in the outcoupling stages such that the intensities $I \propto \frac{1}{d^2}$ are equal in both passes:

$$\frac{I_{\text{second pass}}}{I_{\text{first pass}}} = \frac{T_{\text{out}} T_{\text{in}} p_{\text{scatter}} / d_{\text{second pass}}^2}{1 / d_{\text{first pass}}^2} = 1 \Rightarrow \frac{d_{\text{second pass}}}{d_{\text{first pass}}} = \sqrt{T_{\text{out}} T_{\text{in}} p_{\text{scatter}}} \quad (3.36)$$

This would amount to $\left(\frac{d_{\text{second pass}}}{d_{\text{first pass}}} \right)_y = 0.931 \cdot \sqrt{p_{\text{scatter}}}$ and $\left(\frac{d_{\text{second pass}}}{d_{\text{first pass}}} \right)_{xz} = 0.837 \cdot \sqrt{p_{\text{scatter}}}$.

Magnetic Gradient

The magnetic gradients for the 3-dimensional magneto-optical trap are produced by the Feshbach coils placed next to the glass cell (see chapter 4). Thanks to the high currents that are planned for the Feshbach operation, the coils can generate high gradients upon reversal of the current in one of the coils. As presented in more detail in chapter 4.4, the achievable gradients in the trapping region are ideally $99 \frac{\text{G}}{\text{cm}}$ in the xz axis, where the recapturing axis lies, and even $197 \frac{\text{G}}{\text{cm}}$ along the y axis.

3. The 3-dimensional Magneto-optical Trap

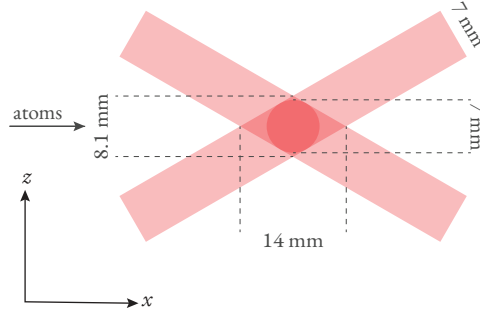


Figure 3.23.: Extent of the trap volume set by the $\frac{1}{e^2}$ -diameters of the three trap laser beams: $2 \cdot 7 \text{ mm} = 14 \text{ mm}$ in x direction, unbounded in y direction, and $\frac{7 \text{ mm}}{\cos 30^\circ} = 8.1 \text{ mm}$ in z direction. If the intensity is kept constant on the second pass through the glass cell by focusing the beam, the beam diameters would be smaller by the factor of at least 0.931 for the y beam and 0.837 for the xz beams (see equation 3.36).

Trap Parameter Estimation

In this section, the properties of the geometry, the trapping light, and the magnetic gradients are used to estimate some benchmarking quantities of the projected 3-dimensional magneto-optical trap.

Trap Dimensions As depicted in figure 3.23, the $\frac{1}{e^2}$ -diameter envelopes of the laser beams outline the trap as a rhomboid shaped region which is 14 mmlong in the recapturing direction (along x), 8.1 mm long along the z axis, and extends over the whole glass cell in y direction.

If the reflection losses on the glass cell surface are compensated for by focusing the beam as suggested in (3.36), the beam diameter and thus also the trap size would decrease to 11.7 mm in x direction, and 6.8 mm in z direction, assuming negligible losses from scattering ($p_{\text{scatter}} \approx 0$).

In addition to that, the atoms recaptured from the atomic beam are subject to a maximum trapping radius depending on their velocity v due to the resonance condition (3.18).

Intensity Estimation Assuming optical powers of about 60 mW for each beam of the 3-dimensional magneto-optical trap (D_2 light), as estimated in figure 3.13, the average intensity in a beam for the magneto-optical trap would amount to $\frac{60 \text{ mW}}{\pi(0.35 \text{ cm})^2} = 156 \frac{\text{mW}}{\text{cm}^2}$ which amounts to a saturation of $s_0 = 31$ for cooler and repumper respectively. Along the recapturing axis (x), this amounts to an effective saturation for the magneto-optical trap of

$$s_{0,3D \text{ MOT, recapturing axis}} = 31 \cdot \cos 30^\circ \cdot 2 = 53 \quad (3.37)$$

(for the cooler and the repumper respectively), where $\cos 30^\circ$ originates from the shallow angles of incidence and the factor of 2 accounts for the fact that both xz beams cool along the recapturing axis. This saturation is large compared to the intensities reported for other trap implementations (cf. section 3.1)

3. The 3-dimensional Magneto-optical Trap

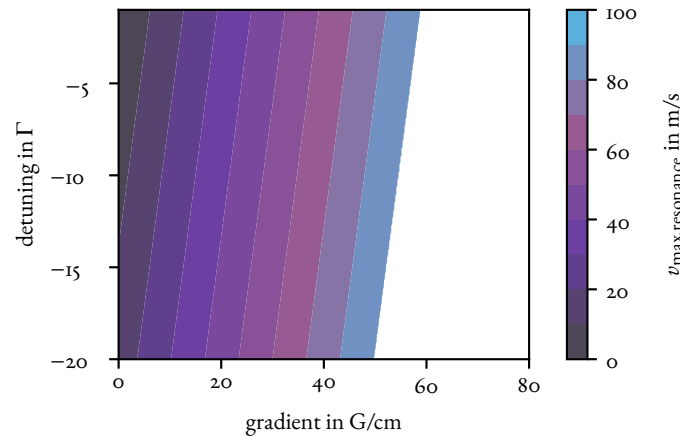


Figure 3.24.: Estimated resonance velocity (3.19) along the recapturing axis x for different detunings δ_{laser} and gradients $\frac{\partial B}{\partial x}$ along the recapturing axis: For a fixed resonance velocity, gradient can be traded for detuning. Resonance velocities higher than the capture velocity of $90 \frac{\text{m}}{\text{s}}$ are cut off (white area). Parameters: $r_{\text{trap}} = 7 \text{ mm}$, $\theta = 30^\circ$.

which means that there is a considerable power overhead for the 3-dimensional magneto-optical trap in the FermiQP demonstrator.

For the gray molasses, the average intensity of the D₁ light would be $\frac{90 \text{ mW}}{\pi (0.35 \text{ cm})^2} = 247 \frac{\text{mW}}{\text{cm}^2}$ which would amount to $s_0 = 16$ for the cooler beam.

Capture and Resonance Velocities For a trap length of 14 mm and saturation $s_0 \gg 1$, so assuming a maximum scattering rate of $\frac{\Gamma}{2}$, the maximum velocity for the small ^6Li atoms recaptured from the atomic beam can be estimated with (3.15):

$$v_{\text{max, capture}} = \sqrt{\frac{\hbar k \Gamma \cdot 14 \text{ mm}}{m}} = 90 \frac{\text{m}}{\text{s}} \quad (3.38)$$

Note that this value is the maximum ideal value for atoms entering the trap exactly along the 14 mm-long center line through the trapping light field. Atoms that are off this line will see a shorter trap radius and thus be constrained by a lesser capture velocity, let alone the diminished light intensity there.

The resonance velocity (3.19) tells which maximum velocity atoms can still have to be on resonance when entering the trap given a certain magnetic gradient and laser detuning $\delta_{\text{laser}} = \omega_{\text{laser}} - \omega_{\text{transition}}$. Atoms faster than that would require even further detuned light to be on resonance. The resonance velocity is mapped in figure 3.24 outlining how gradient and detuning can be traded for each other at fixed resonance velocities. E.g., for $\delta_{\text{laser}} = -5\Gamma$, a gradient of $57 \frac{\text{G}}{\text{cm}}$ would be required to reach $v_{\text{max, resonance}} \approx v_{\text{max, capture}}$.

Ch 3 proof-reading run 1 until here

4. Feshbach and Gradient Field Coils

In this chapter, the geometry and design and characterization of the coils used for creating steep magnetic gradients for the 3-dimensional magneto-optical trap and a strong homogeneous magnetic fields for tuning Feshbach resonances is presented. In addition to that, a Python library developed for simulating the magnetic fields and gradients generated by the coils as well as certain characteristics of them is presented. These coils are called *Feshbach coils* in this chapter.

unify terminology:
Helmholtz configuration = geometry,
Feshbach mode = current,
gradient mode = current

4.1. Requirements and Constraints

In this section, all requirements and constraints in terms of field strength, geometry, stability and field curvature for the coils are presented.

Magnetic Field Strength

The Feshbach coils serve two main purposes in the FermiQP demonstrator. On the one hand, they provide magnetic gradients on the order of $1 \times 10^1 \frac{\text{G}}{\text{cm}}$ to $1 \times 10^2 \frac{\text{G}}{\text{cm}}$ for the 3-dimensional magneto optical trap. On the other hand, they need to produce homogeneous magnetic fields for scanning over the Feshbach resonance of lithium at 832 G. A maximum field of 1300 G, created at a current of $I = 400 \text{ A}$, was set as a target for the coil setup.

In order to generate these homogeneous fields, the coils are arranged in Helmholtz configuration, meaning that two equally-sized circular coils are placed on a common axis such that their distance is equal to their radius.¹ The effective ratio of distance and radius required for homogeneous fields, however, depends on the finite size of the coils.

¹In the rest of this chapter, the term *Helmholtz configuration* will refer to two coils of the same size sharing the same axis at a distance equal to their radii. The coil arrangements discussed in this chapter will be in Helmholtz configuration. If the current in both coils flows in the same direction, meaning that the coils generate a homogeneous field between them, the operation mode will be referred to as *homogeneous field mode* or *Feshbach mode* interchangeably. If, however, the current flows in mutually inverted directions such that the coils generate a field gradient between them, the operation mode will be referred to as *gradient mode*. Note that, similar to the $d = r$ condition of the Helmholtz configuration, there is an optimal configuration for gradient fields, often called *anti-Helmholtz configuration*, which however requires a different distance $d \neq r$ and does not occur in this chapter.

4. Feshbach and Gradient Field Coils

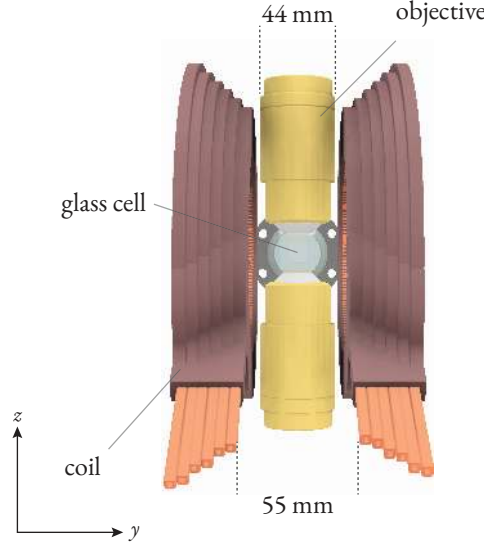


Figure 4.1.: Position of the Feshbach coils with respect to the glass cell and the objectives: The objectives (44 mm diameter) which are positioned below and above the glass cell are enclosed by the two coils, setting the minimum distance between the coils. The innermost coil wires have a distance of 55 mm.

Geometry

In order to produce the high Feshbach fields in the glass cell with reasonable currents, the radius of the coils should be kept as small as possible, and they should be placed as close to the glass cell as possible.

The coils will enclose the two objectives sitting above and below the glass cell between them. This introduces a minimum distance of around 50 mm between the coils still allowing a few mm of leeway to fit the objectives between the coils. It was decided for a distance of 55 mm between the innermost wires of the coils, not considering additional surface material on the coils. These geometrical constraints allow an estimation of the number of windings needed to attain the required 1300 G of field in Helmholtz configuration to 30, which was determined using simulations (see sections 4.2 and 4.3).

The orientation of the coil arrangement is constraint by the requirement to drive Raman transitions on the atoms in the optical lattice with π -polarized light shone in through the objectives. π transitions can only be driven with light having a polarization parallel to the quantization axis of the atoms, which is set by the direction of the magnetic field. Light shone in along the z axis through the objectives can only be π -polarized in the xy plane, constraining the direction of the magnetic field to the xy plane. It was decided to align the coil arrangement axis with the y axis of the experiment chamber, meaning that the two coils sit on the left and on the right of the glass cell with the coil axis passing through the trap region of the magneto-optical trap.

Figure 4.1 shows the geometrical constraints on the position of the coils.

4. Feshbach and Gradient Field Coils

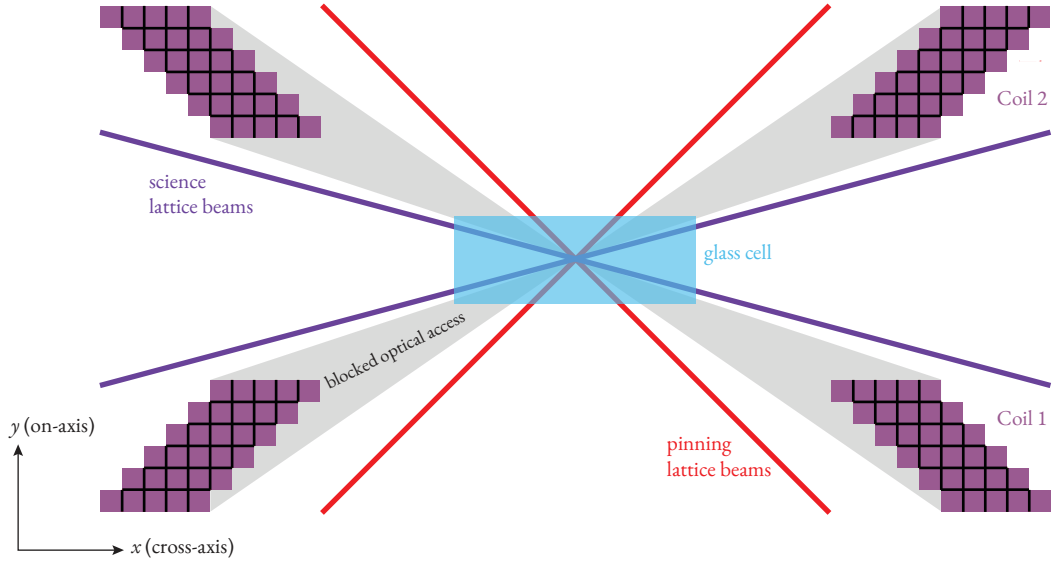


Figure 4.2.: Parallelogram-shaped cross-section of the coils for minimizing the blocked optical access into the glass cell, letting the pinning and science lattice beams pass alongside the coil (view from above): The windings layers stacked onto each other (in the coil axis direction) have radii that increase by one wire size per layer (cross-axis direction).

As the coils have many windings, thus having a significant size, and are close to the glass cell, they block a significant part of the optical access to the location of the atoms. Many laser beams and imaging signals must, however, be shot into and received from the glass cell, demanding that the coils leave open as much optical access to the glass cell as possible. Most notably, the beams of the magneto-optical trap need to enter the glass cell on the y axis through the left and right surfaces, the pinning lattice beams also enter there with incidence angles of $\pm 45^\circ$. On the short side of the glass cell, the science lattice beams enter with incidence angles of around $\pm 15^\circ$. The available space for the coils is hence bound by these laser beams. In order to minimize the blocked optical access, a cone-shape coil geometry with parallelogram-shaped cross-section, consisting of 6×5 windings, was opted for, as depicted in figure 4.2. The opening angle of the cone has been set to 45° because then the Helmholtz condition of equal coil distance and radius is approximately fulfilled for every layer.

Field and Temperature Stability

The FermiQP demonstrator aims for a relative field stability of 10^{-7} calling for an active stabilization mechanism. For this purpose, both coils are independently driven by two independent power supplies enabling fast switching.

Furthermore, it is important to ensure thermal stability of the coils. The electrical power $P(I) = RI^2$ dissipated in the coils with resistance R shows quadratic scaling with the driving current I . For an exemplary coil with $10 \text{ m}\Omega$ resistance driven with $I = 400 \text{ A}$ this would amount to a dissipated power of 1.6 kW converted into heat. In order to transport this heat off efficiently, avoiding a critical increase

4. Feshbach and Gradient Field Coils

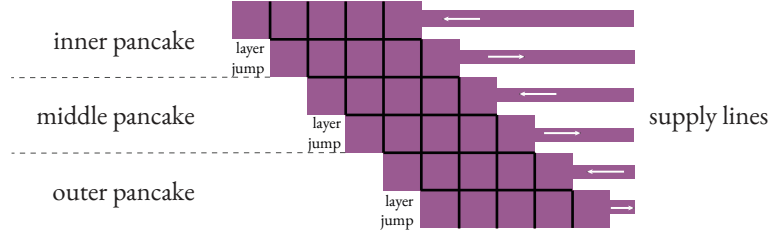


Figure 4.3.: Cross-section of the pancake structure of the coils: Two layers of wire are combined into a so-called pancake that constitutes a single water cooling circuit. The layers have layer jump on the innermost winding where the wire hops from one layer to the other. The current in the two supply lines for each pancake is flowing in opposite directions such that the magnetic fields originating from the wire cancel out in the far-field.

of temperature, the coil must be made of hollow-core wires allowing for water-cooling. For a given maximal temperature increase ΔT of the cooling water, the cooling power of the water can be estimated as

$$Q_{\text{cool}} = c_{\text{water}} \Delta T m_{\text{water}} v_{\text{flow}} \quad (4.1)$$

with the heat capacity c_{water} of water, the specific mass m_{water} , and the speed v_{flow} of the cooling water flow, which depends on the applied pressure, the turbulence of the flow, and the wire geometry.

To lower the required cooling water pressure and to avoid turbulences in the cooling water stream, it was decided to separate the wire layers of the coils into pancakes of two layers each constituting separately driven water cooling circuits, as shown in figure 4.3. For this the two supply lines for each pancake are placed next to each other, forming pairs of wires with current flowing in opposite directions. This has the additional advantage that the fields of the supply lines cancel out in the far-field and do not influence the magnetic field in the center of the coil arrangement.

Field Curvature

When the atoms trapped in the optical lattice are exposed to the homogeneous Feshbach field, they experience an energy shift resulting from the interaction of the magnetic moment $\vec{\mu}$ with the field that can lead to trapping or anti-trapping effects \vec{B} [15, 29, 30]:

$$E_{B, \text{high-field seeker}} = \mp \vec{\mu} \vec{B} \quad (4.2)$$

where the sign of the shift depends on whether the atoms are in high- or low-field seeking states. The magnitude of the magnetic moment is $\mu \approx \mu_B$ with the Bohr magneton $\mu_B = 9.27 \times 10^{-24} \frac{\text{J}}{\text{T}}$.

In the very center of the coil arrangement, the magnetic field in the Helmholtz operation mode of the coils is completely homogeneous. Realistically, however, there is a non-negligible position dependence

4. Feshbach and Gradient Field Coils

$B(\vec{r})$ of the field, stemming from the finite size of the region of interest and imperfections in positioning, aligning, and manufacturing of the coils. This leads to a position-dependent potential that the atoms are exposed to:

$$\hat{H}(\vec{r}) = \frac{\vec{p}^2}{2m} \mp \vec{\mu} \vec{B}(\vec{r}) \quad (4.3)$$

Assuming that the magnetic field around the center of the coil arrangement follows a paraboloid shape, in one dimension $B(q) = B_0 + a_q q^2$ with a field curvature coefficient a and a spatial coordinate q , one can identify the magnetic potential with a quantum mechanical harmonic oscillator:

$$\underbrace{V_0 + \frac{1}{2} m \omega^2 q^2}_{V_{\text{HO}}(q)} \equiv \underbrace{\mp \mu B(q) = \mp \mu B_0 \mp \mu a_q q^2}_{V_{\text{magnetic}}(q)} \quad (4.4)$$

Identifying the position-dependent terms, the magnetic potential can be assigned the angular trap frequency $\omega_{\vec{q}}$ along the \vec{q} coordinate axis:

$$\omega_{\vec{q}} = \sqrt{\mp \frac{2\mu a_{\vec{q}}}{m}} = \sqrt{\mp \frac{2\mu_B a_{\vec{q}}}{m}} \quad (4.5)$$

In the following, the trapping potential is considered trapping in the \vec{q} direction if $\omega_{\vec{q}}$ is real, and anti-trapping if $\omega_{\vec{q}}$ is imaginary. For high-field seekers, the potential is trapping if $a_{\vec{q}} < 0$ and anti-trapping if $a_{\vec{q}} > 0$. For low-field seekers, the potential is trapping if $a_{\vec{q}} > 0$, and anti-trapping if $a_{\vec{q}} < 0$. This can be intuitively seen as high-field seekers are trapped if the field is concave and has a maximum, hence $a_{\vec{q}} < 0$, and the other way around for low-field seekers.

In a two-coil field, if the potential is trapping along the arrangement axis, it is anti-trapping in the cross-axis directions, and vice versa. This is due to Earnshaw's theorem [31] stating that a magnetic field in three dimensions has the shape of a hyperboloid, and thus cannot have a global extremum rather than a saddle point. This implies that the magnetic field is curved into opposite directions on two axes as shown in figure 4.4. The field in the coil-axis direction is curved twice as much as in the cross-axis direction: $\frac{a_{\text{on-axis}}}{a_{\text{cross-axis}}} = -2$, hence the trap frequencies have a ratio of $\frac{|\omega_{\text{on-axis}}|}{|\omega_{\text{cross-axis}}|} = \sqrt{2}$ [30] (see also figure 4.10 in section 4.4).

Note that $a_{\vec{q}}$ relates to the field landscape along \vec{q} as $a_{\vec{q}} = \frac{1}{2} \frac{\partial^2 B}{\partial q^2}$ which can be seen from the Taylor expansion $B(q) = B|_0 + \left. \frac{\partial B}{\partial q} \right|_0 q + \frac{1}{2} \left. \frac{\partial^2 B}{\partial q^2} \right|_0 q^2 + O(q^3)$ around 0 identifying the second order term with $a_{\vec{q}} q^2$.

The design goal for the coil arrangement with regard to the field curvature is to minimize the absolute trap frequency in each direction by setting the coil distance accordingly.

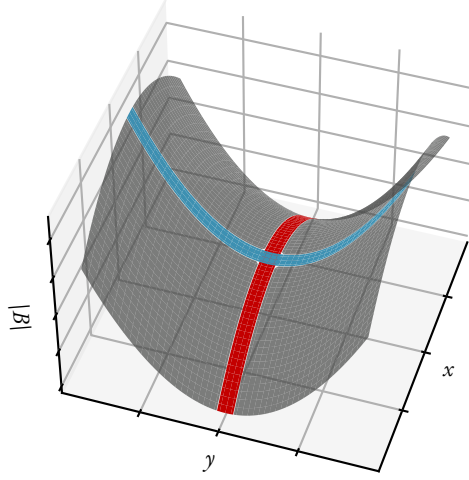


Figure 4.4.: Field curvature around the center of a homogeneous field: While on one axis, the curvature is positive (here along y (blue), anti-trapping for high-field seekers), it is negative on the other axis (here along x (red), trapping for high-field seekers).

4.2. Simulation

In order to determine the optimal specifications and to characterize the coils, a simulation python library was developed (called *coil simulation library* from now on). It makes heavy use of the magnetic field library *magpylib* [32, 33] providing magnetic field vectors at arbitrary positions originating from wire loops, straight wires and permanent magnets of different shapes only from analytic calculations.

Modelling

The *coil simulation library* models arrangements of two or more coils sharing a common axis. The models are parameterized by the distance d_{coil} of the coils to the center, the number n_{coil} , the radius r_{coil} , and the arrangement geometry of the windings of each coil, the spacing w between the windings, the geometry of the wire, presence and length of supply lines, and the current I_{coil} flowing in each coil and even in each winding if desired.

A coil is modelled as a set \mathcal{C} of circular wire loops $L(r, y, I)$ with radius r_i , a center y position y , and current I . As is the case for the FermiQP demonstrator, the wire loops' axes are parallel to the y axis. For the $n_{\text{on-axis}} = 6$ on-axis windings and the $n_{\text{cross-axis}} = 5$ cross-axis windings, each loop L_{ac} with on-axis index $a \in \{0, \dots, n_{\text{on-axis}} - 1\}$ and cross-axis index $c \in \{0, \dots, n_{\text{cross-axis}} - 1\}$ is defined as

$$L_{ac} = L(r_{\text{coil}} + r_{ac}, y_{\text{coil}} + y_{ac}, I_{\text{coil}}) \quad (4.6)$$

4. Feshbach and Gradient Field Coils

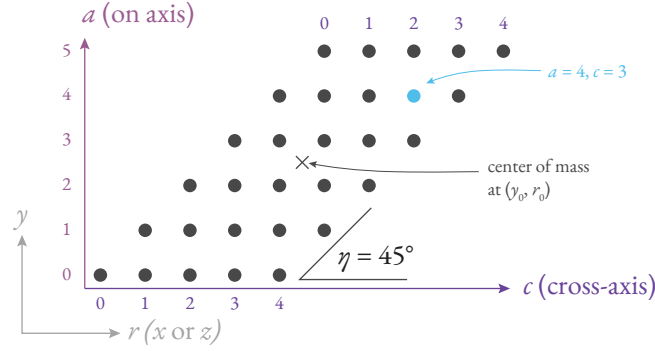


Figure 4.5.: Modelling a coil as a set of wires with on-axis indices a and cross-axis/radial indices c (counted from 0). The different layers along the axis enclose an angle η . In the case of the coils for the FermiQP demonstrator with 6×5 windings, a corresponds to the y axis, and c corresponds to the radial xz plane, and the angle η is 45° . The winding ($a = 3, c = 2$) is exemplarily highlighted, according (4.7) and (4.8) it lies at $(y = y_0 + \frac{3}{2}w, r = r_0 + \frac{5}{2}w)$.

with the on-axis (y) and radial (cross-axis) offsets

$$y_{ac} = w \cdot \left(a - \frac{n_{\text{on-axis}}}{2} + \frac{1}{2} \right) \quad (4.7)$$

$$r_{ac} = y_{ac} \tan \eta + w \cdot \left(c - \frac{n_{\text{cross-axis}}}{2} + \frac{1}{2} \right) \quad (4.8)$$

where w is the side length of a wire, and η is the opening angle of the parallelogram-shaped cross-section of the coil cone ($\eta = 45^\circ$ for the coils in the FermiQP demonstrator). Figure 4.5 visualizes how a coil is modelled as a set of wires.

This way of modelling a coil neglects the spiral shape of the coil wire as well as the jump between different on-axis layers of the coil.

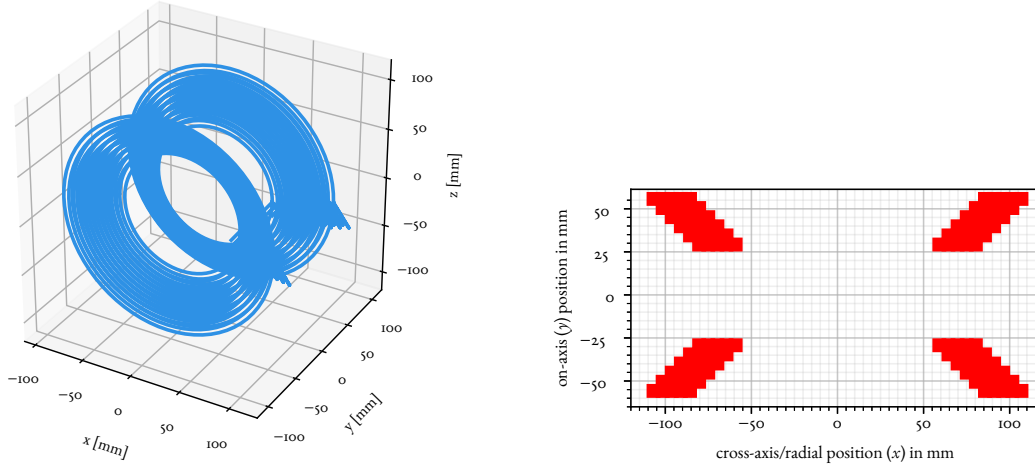
For an arrangement, the library provides the user with magnetic field vectors and magnitudes at arbitrary positions, plots of fields along trajectories through the arrangement, maps of the field landscape in planes in the arrangement, information about gradients and curvatures of the fields, resistances, inductances, dipole moments, $\frac{L}{R}$ time constants, mutually exerted mechanical forces of the coils, and sketches of the arrangement (see figure 4.6 for exemplary sketches for the Feshbach coils).

The technical details of the implementation of the *coil simulation library* are outlined in appendix chapter B. The following paragraphs explain how important characteristics of the coils and fields are calculated in the *coil simulation library*.

Coil properties

The *coil simulation library* provides the following fundamental coil properties:

4. Feshbach and Gradient Field Coils



(a) 3-dimensional sketch of the coil arrangement, modelled as individual circular windings (generated with *magpylib* [33])

(b) Sketch of the cross-section of a single coil

Figure 4.6.: Sketches of the Feshbach coils of the FermiQP demonstrator as generated by the *coil simulation library*

Resistance The resistance R of a coil is determined using the specific resistance of copper of $\rho_{\text{copper}} = 1.72 \times 10^{-8} \Omega \text{ m}$:

$$R_C = \frac{\rho_{\text{copper}} \sum_{L \in C} 2\pi r_L}{w^2 - A_{\text{hollow}}} \quad (4.9)$$

with the cross-section area A_{hollow} of the hollow wire.

Inductance and L/R time The inductance of a coil can be determined as $L = \frac{\Phi}{I}$ with the magnetic flux $\Phi = \int B dA$ at a current I [34]. In the *coil simulation library*, the flux through a wire loop L is approximated as $\Phi_L \approx B \cdot \pi r_L^2$ with the total magnetic field B . The total inductance of coil L is calculated as

$$L_C = \sum_{L \in C} \frac{B(y = y_L) \pi r_L^2}{I_L} \quad (4.10)$$

For calculating the self-inductance, B was set to the field solely generated by the respective coil. For estimating the inductance of the coil when part of an arrangement of coils, B was set to the field of the whole arrangement. This leads to higher inductances when operated in Helmholtz configuration and lower inductances when operated in gradient configuration. This in-arrangement inductances are

4. Feshbach and Gradient Field Coils

only meaningful if the amount of current flowing in all coils is the same and coupled, and if the coils have the same geometry.²

The time constant $\tau = \frac{L}{R}$ quantifies how fast the current in a coil with inductance L and resistance R can be switched by a sudden change of the applied voltage: $\Delta I(t) \propto 1 - \exp(-\frac{t}{\tau})$ [34]. In the *coil simulation library*, this time constant is estimated as

$$\tau_C = \frac{L_C}{R_C}. \quad (4.11)$$

Using the inductance of the whole arrangement in Helmholtz configuration for L increases the estimated τ , as the inductance of the whole arrangement of coils with coupled currents is higher and hence has a longer switching time. For the arrangement in gradient mode, the estimated τ is decreased as the coils' mutual inductance effects have opposite sign.

Dipole moment The magnetic dipole moment \vec{m} of a coil determines the force $\vec{F} = \vec{m}(\vec{\nabla} \vec{B})$ and torque $T = \vec{m} \times \vec{B}$ it experiences in a magnetic field. Furthermore, the magnetic field generated on the coil axis (y) by a magnetic moment \vec{m} amounts to $\vec{B} = \frac{\mu_0 \vec{m}}{2\pi y^3}$ in the far-field ($y \gg r$). For a wire loop, it is defined as $\vec{m} = I \vec{A}$ with the coil axis vector \vec{A} having the length of the wire loop cross-section area [35]. In the *coil simulation library*, the magnetic moment of a coil arrangement \mathcal{A} is calculated as

$$m_{\mathcal{A}} = \sum_{L \in \mathcal{A}} I_L \cdot \pi r_L^2. \quad (4.12)$$

Field properties

The *coil simulation library* provides the following properties of the field generated by an arrangement:

Curvature and Trap Frequency The field curvature a_q along an axis q in an arrangement \mathcal{A} , as defined in chapter 4.1, is calculated from sampled magnetic field strength values $B_i(\vec{0} + d \cdot \vec{q})$ for distances d from the center along the \vec{q} axis. In the *coil simulation library*, the curvature is determined in a region of ± 3.5 mm around the center in 200 steps as a default. A degree-7 polynomial $\hat{B}(d) = \sum_{i=0}^7 c_i d^i$ is fit to the sampled data. The curvature is then the second coefficient of the fit: $a_{\vec{q}} = \hat{c}_2$.

add factor, see Demtroder 2 ch 4.3.2.2

Verify, does the L modelling and the conclusions for τ make sense?

²With coupled currents in the individual coils, the whole arrangement can be thought of as a single coil consisting of multiple sub-coils at different positions. The self-inductance of the arrangement is then calculated with the total magnetic field produced by all sub-coils of the arrangement, and can be thought of as a sum of the individual inductances of the sub-coils.

4. Feshbach and Gradient Field Coils

The high-field seeker trap frequency is then calculated as (cf. equation 4.5)

$$f_{c\mathcal{A}, \vec{q}, \text{high-field seeker}} = \frac{1}{2\pi} \sqrt{\left| \frac{2\hat{c}_2\mu_B}{m_{\text{Li}}} \right|} (-\text{sgn}\hat{c}_2) \quad (4.13)$$

which is positive if the field is trapping and negative if anti-trapping for high-field seekers along \vec{q} .

Gradient The gradient in an arrangement $c\mathcal{A}$, meaning the linear components of the field landscape, along \vec{q} is determined from the same polynomial fit as for the curvature.

$$g_{c\mathcal{A}, \vec{q}} = \left. \frac{\partial B}{\partial q} \right|_{q=0} = \hat{c}_1 \quad (4.14)$$

Mechanical Force The axial mechanical force on a coil C in the field of an arrangement is estimated using its magnetic moment and the field gradient: $\vec{F} = \vec{m}(\vec{\nabla}\vec{B})$. As the magnetic moment only has a y component, only the axial gradient of the field is relevant. For calculating the force on the total coil, its wire loops' magnetic moments $m_L = I_L \cdot \pi r_L^2$ multiplied by the approximated y gradient $\left. \frac{\partial B}{\partial y} \right|_{y=y_L} \approx \frac{B(y_L+s) - B(y_L)}{s}$, with a default step length $s = 0.5$ mm, are summed:

$$F_C \approx \sum_{L \in C} m_L \cdot \left. \frac{\partial B}{\partial y} \right|_{y=y_L} \approx \sum_{L \in C} I_L \pi r_L^2 \left(\frac{B(y_L + s) - B(y_L)}{s} \right) \quad (4.15)$$

This approximation is coarse, not only because of the approximation of the gradient, but especially because the finite radial extent of the coil was neglected, meaning that the coil was assumed to be small compared to the radial distance on which the y gradient changes.

check validity

4.3. Coil Properties

In this section, an overview of the geometrical specifications and the operational properties of the Feshbach coils for the FermiQP demonstrator is given. Also, the field generated by a single coil is characterized.

Geometry

The coils were produced by an external producer (Krämer Energietechnik, Am Escheberger Weg 8a, 34289 Zierenberg, Germany). In consultation with them, the required specifications were determined using the *coil simulation library* optimizing field curvature and peak field in Helmholtz configuration. In total, three coils were purchased, two for operation in the demonstrator and one spare. They are called *Gauss*, *Maxwell*, and *Tesla*.

4. Feshbach and Gradient Field Coils

	specified	<i>Gauss</i> (mm)	<i>Maxwell</i> (mm)	<i>Tesla</i> (mm)
center-of-mass radius	83 mm			
diameter of layer 1 (inner)	116 mm	115.5 ± 0.1	115.1 ± 0.2	115.3
diameter of layer 2 (inner)	126 mm			
diameter of layer 3 (middle)	136 mm			
diameter of layer 4 (middle)	146 mm			
diameter of layer 5 (outer)	156 mm	155 ± 1	156 ± 1	156 ± 1
diameter of layer 6 (outer)	166 mm	166 ± 1	165 ± 1	165 ± 1
height of layer 1 (wire & coating)	6.5 mm	6.7 ± 0.1	6.7 ± 0.2	6.8 ± 0.1
height of layers 2 - 5 (wire)	5.5 mm	5.6 ± 0.1	5.8 ± 0.2	5.6 ± 0.1
height of layers 6 (wire & coating)	6.5 mm	6.7 ± 0.1	6.8 ± 0.1	6.9 ± 0.1
total height	35 mm	35.8 ± 0.3	35.3 ± 0.3	35.5 ± 0.3
total wire side length	5.3 mm	5.2 ± 0.1	5.2 ± 0.1	5.2 ± 0.1
wire copper material side length	5.0 mm			
wire insulation thickness	0.15 mm			
wire hollow core diameter	3.0 mm			

Table 4.1.: Geometrical properties of the Feshbach coils: The first column gives the specified value, for some quantities the measured values are given for the three coils *Gauss*, *Maxwell*, and *Tesla* (epoxy coating included).

A center-of-mass radius of 83 mm was decided for. The six layers with five windings each are grouped into three pancakes (outer, middle, and inner). Each pancake has two supply lines that all connect to the coil at the same azimuthal point. All other geometrical specifications as well as some measured geometrical properties on the three coils are listed in table 4.1.

Figure 4.7a shows how in the cross-section of a coil the wire layers are coating in epoxy material. Figure 4.7b shows the specification of the used wire of 5.3 mm width, 0.3 mm of which are accounted for by the Kapton insulation, with a hollow core of 3.0 mm diameter. Figures 4.7a and 4.8b show 3-dimensional drawings of the specified coils.

The coils are held in place using holders designed by the engineering department of the Max Planck Institute of Quantum Optics, made out of the non-magnetic material PEEK. Massive spacers between the two coils ensure that they cannot change their distance due to any gradient forces, and they impede vibrations by tightly fixing the coils.

Operational Properties

The operational properties introduced in section 4.2 were simulated using the *coil simulation library* and are listed in table 4.2.

4. Feshbach and Gradient Field Coils

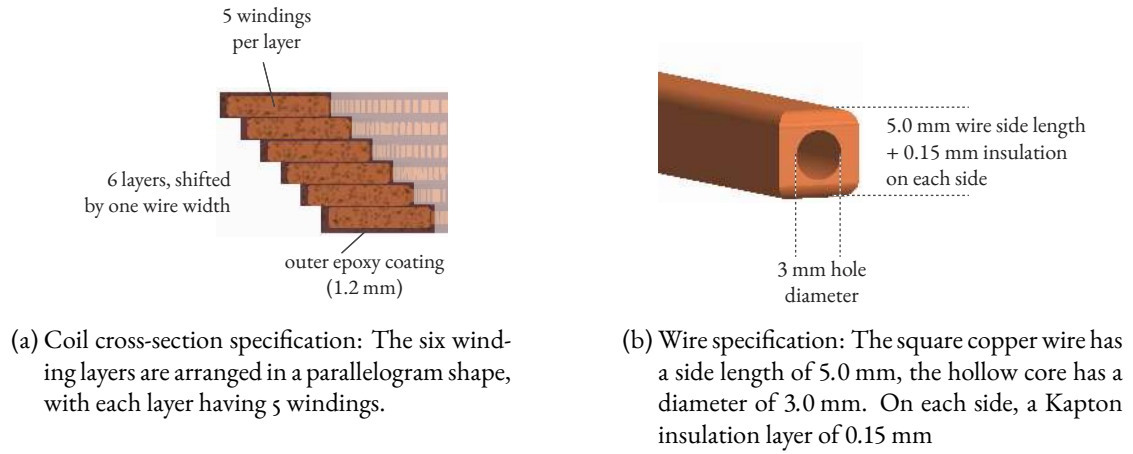


Figure 4.7.: Cross-section geometry and wire specification

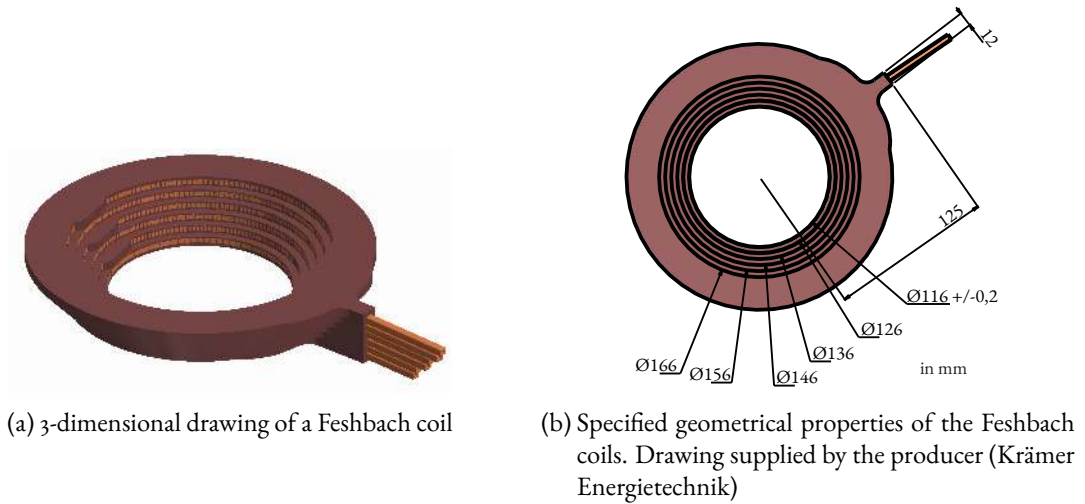


Figure 4.8.: Geometry of a Feshbach coil

4. Feshbach and Gradient Field Coils

quantity	simulated value	equation reference
wire length	15.7 m	
resistance R_C	14.9 m Ω	(4.9)
inductance L_C	0.15 mH	(4.10)
time constant τ_C	9.9 ms	(4.11)
magnetic dipole moment m_C	265 A m ²	(4.12)

Table 4.2.: Operational properties of the Feshbach coils determined using the coil simulation library

In a four-point measurement, the resistance of the middle pancake of the *Gauss* coil (wire length roughly 15.7 m/3) with estimated 6 m of supply line wire was measured to be 12.8 m Ω . The expected value of $\rho_{\text{copper}} \cdot \frac{(5 \text{ mm})^2 - \pi(1.5 \text{ mm})^2}{15.7 \text{ m}/3 + 6 \text{ m}} \approx 11 \text{ m}\Omega$ is on the same order of magnitude. The experimenters reckon that the resistance might be higher than expected from the simulation due the bends of the wire.

Too vague
to be in
here?

Additionally, the coil was set up to form an LC circuit together with an oscilloscope of $C = 15 \text{ pF}$ to verify the simulated inductance of 15 mH. In this setup, the supply lines of the coil were also wound up to coils of 9 windings with a radius of about 11 cm, leading to an estimated extra inductance of $L_{\text{supply}} = \frac{N\Phi}{I} = \frac{N^2\mu_0\pi r}{2} \approx 0.02 \text{ mH}$. The resonance frequency of the circuit was experimentally determined as $f = 3.19 \text{ MHz}$ which allows to estimate the inductance of the coil:

$$f = \frac{1}{2\pi\sqrt{(L_{\text{coil}} + L_{\text{supply}})C}} \Rightarrow L_{\text{coil}} = \left(\frac{1}{2\pi f\sqrt{C}} \right)^2 - L_{\text{supply}} \approx 0.15 \text{ mH} \quad (4.16)$$

which corroborates that the simulated value is realistic.

Magnetic Fields

Using a Sensys FGM3D/1000 fluxgate magnetic field probe (dominant relative error of 0.5 %), the on-axis magnetic field produced by the three coils *Gauss*, *Maxwell*, and *Tesla* at $I = 1.000 \text{ A}$ was mapped and is displayed in figure 4.9. In addition to that, the fields were fit to the following model the on-axis field of 30 partially separated wire loops [35]:

$$\hat{B}[I, r, y_0](y) = \sum_{a=0}^5 \sum_{c=0}^4 \frac{\mu_0 I}{2} \frac{r_{ac}^2}{(r_{ac}^2 + (y - y_{ac})^2)^{\frac{3}{2}}} \quad (4.17)$$

with the position $y_{ac} = y_0 + (a - 2.5)w$ and the radius $r_{ac} = r + (c - 2)w$ of a winding with on-axis index a , cross-axis index c , and a winding spacing w .

With root means square error $RMSE[B, \hat{B}] = \sqrt{\frac{1}{N} \sum_{i=1}^N (B_i - \hat{B}_i)^2}$ values of $< 3 \text{ mG}$, which is about 10^{-3} of the maximum field, the model fits the observed field landscapes very well. The resulting pa-

4. Feshbach and Gradient Field Coils

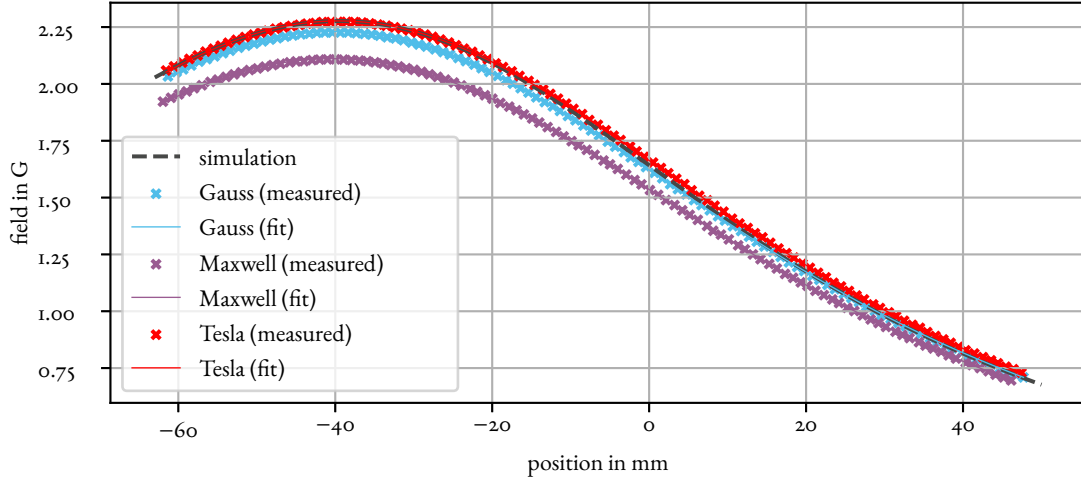


Figure 4.9.: Simulated on-axis fields and measured on-axis fields of the coils *Gauss*, *Maxwell*, and *Tesla* for $I = 1.000$ A. Position 0 mm is the projected center point between two coils. While *Tesla*'s field matches the simulation best, *Gauss*'s is a little weaker, and *Maxwell*'s is substantially less than expected.

rameters \hat{I} , \hat{r} , and \hat{y}_0 are listed in table 4.3.³ One can conclude that the coils cannot produce the same maximum field and that they act like they are operated at different currents and/or have slightly different dimensions. Comparing the measured and the simulated fields with $RMSE[B, B_{\text{simulated}}]$ (see table 4.3), one can also see that *Tesla* matches the expected field landscape best, followed by *Gauss*, and *Maxwell* very far off.

In order to investigate the origin of this problem, the individual pancakes of all coils were characterized with respect to the maximum field they produce at $I = 1.000$ A, as listed in table 4.4. The values show that even the respective outer, middle, and inner pancakes of the individual coils differ significantly in terms of the magnetic fields they produce.

These differences between the coils could originate from geometrical irregularities introduced during the manufacturing process, electrical shorts (which are rather unlikely considering that every pancake would be affected), the layer jumps, or other imperfections. During the writing of this thesis, the reason of these deviances could not be clearly identified. The different fields and geometrical scales of the coils need to be taken into account when setting the coil distance and the respective operating currents for getting a flat and curvature-free homogeneous field. *Gauss* and *Tesla* were chosen as the coils to be used for the implementation of the Feshbach and gradient fields as they fulfill the expectations best.

³ \hat{I} and \hat{r} are highly correlated (99.9976%), which can be attributed to $\hat{B} \propto \frac{I}{r^2}$. This means that

I and r very collinear and hence highly exchangeable. Quality of fit does not come from variance in z , but from the non-linear shape of the curve.

4. Feshbach and Gradient Field Coils

	<i>Gauss</i>	<i>Maxwell</i>	<i>Tesla</i>	simulation
\hat{I} in A	0.97 ± 0.00	0.93 ± 0.00	0.98 ± 0.00	1.00
\hat{r} in mm	80.99 ± 0.13	81.90 ± 0.14	80.66 ± 0.13	83.00
\hat{y}_0 in mm	-40.03 ± 0.10	-40.41 ± 0.10	-39.54 ± 0.10	-42.50
$RMSE[B, \hat{B}]$ in mG	2.73	2.14	2.69	
$RMSE[B, B_{\text{simulation}}]$ in mG	31.20	121.19	17.30	

Table 4.3.: Results for the on-axis magnetic field model parameters \hat{I} , \hat{r} , and \hat{y}_0 in equation (4.17) for *Gauss*, *Maxwell*, and *Tesla*, operated at $I = 1.000$ A: All coils act as if they are operated with different currents and/or have different geometries. While *Gauss* and *Tesla* are still quite close to the expected fields, which can be seen from the $RMSE$ between the measured fields B and the simulated fields $B_{\text{simulation}}$, *Maxwell* is far off the expectations. For all coils, the fits match the measured fields very well, which can be seen from $RMSE[B, \hat{B}]$.

pancake	coil	y_{max}	B_{max}
outer	<i>Gauss</i>	(-56 ± 1) mm	0.689 G
	<i>Maxwell</i>	(-57 ± 1) mm	0.622 G
	<i>Tesla</i>	(-55 ± 1) mm	0.658 G
middle	<i>Gauss</i>	(-42 ± 1) mm	0.762 G
	<i>Maxwell</i>	(-46 ± 1) mm	0.715 G
	<i>Tesla</i>	(-44 ± 1) mm	0.773 G
inner	<i>Gauss</i>	(-31 ± 1) mm	0.813 G
	<i>Maxwell</i>	(-31 ± 1) mm	0.804 G
	<i>Tesla</i>	(-32 ± 1) mm	0.879 G

Table 4.4.: Maximum fields of the individual pancakes of *Gauss*, *Maxwell*, and *Tesla* at a current of 1.000 A: The maximum field generated is substantially different for each coil even on when regarding single pancakes.

4. Feshbach and Gradient Field Coils

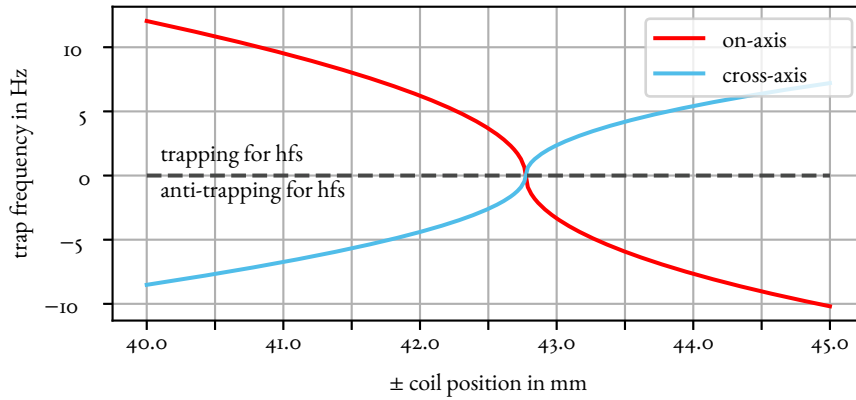


Figure 4.10.: Dependency of the trap frequency on the position of the Feshbach coils (calculated from data simulated with the *coil simulation library*, positive trap frequencies denote a trapping, negative an anti-trapping potential for high-field seekers): If the coils are positioned ± 42.8 mm away from the arrangement center, the absolute trap frequency becomes minimal for both the on-axis and cross-axis/radial directions. For positions close and farther from the center, it can be seen that, if one axis is trapping, the other is always anti-trapping, with a ratio of trap frequencies of $-\sqrt{2}$.

4.4. Field Characterization

In this section, the fields of an arrangement of two coils in Helmholtz configuration is simulated and optimized in terms of coil position and operating current taking into account the determined properties of the single coils.

more concise, shorter sentences

Homogeneous Field

As a first step, the homogeneous field (coils in Helmholtz/Feshbach configuration) was characterized with respect to its curvature and the field landscape between the coils. Then the measured field landscapes for the coils *Gauss* and *Tesla* were used to optimize the operating current and positions for both coils.

Trap frequencies The expected trap frequency of the arrangement of coils was determined with the *coil simulation library* for different coil positions. As can be seen from figure 4.10, the optimal position of (the center of mass of) the coils where the absolute trap frequencies are minimal in both on-axis and cross-axis direction is at about 42.8 mm.

Field landscape The simulated field landscape in this optimal configuration of the coils is mapped in figure 4.11a, the fields along the coil axis and the cross-axis are displayed in figures 4.11b and 4.11c.

4. Feshbach and Gradient Field Coils

quantity	simulated value	equation reference
center field B_{\max}	1309 G	
center field per current $\frac{B}{I}$	$3.27 \frac{\text{G}}{\text{A}}$	
inductance $L_{\mathcal{A}}$	0.20 mH	(4.10)
time constant $\tau_{\mathcal{A}}$	13.3 ms	(4.11)
magnetic dipole moment $m_{\mathcal{A}}$	530 A m^2	(4.12)
axial force $F_{\mathcal{A}}$	193 N	(4.15)

Table 4.5.: Properties of the coil arrangement in Helmholtz/Feshbach configuration and of the produced fields (simulated using the *coil simulation library*)

The maximum field at the center in this configuration is 1309 G. Table 4.5 lists some properties of the arrangement and its field in Helmholtz/Feshbach configuration.

Optimization of Current and Position The observed difference in the measured field landscapes of *Gauss* and *Tesla* (see figure 4.9), which are to be used for implementing the coil arrangement, call for an optimization of their respective position and current such that the curvature of the Feshbach field is minimal and has as little gradient as possible.

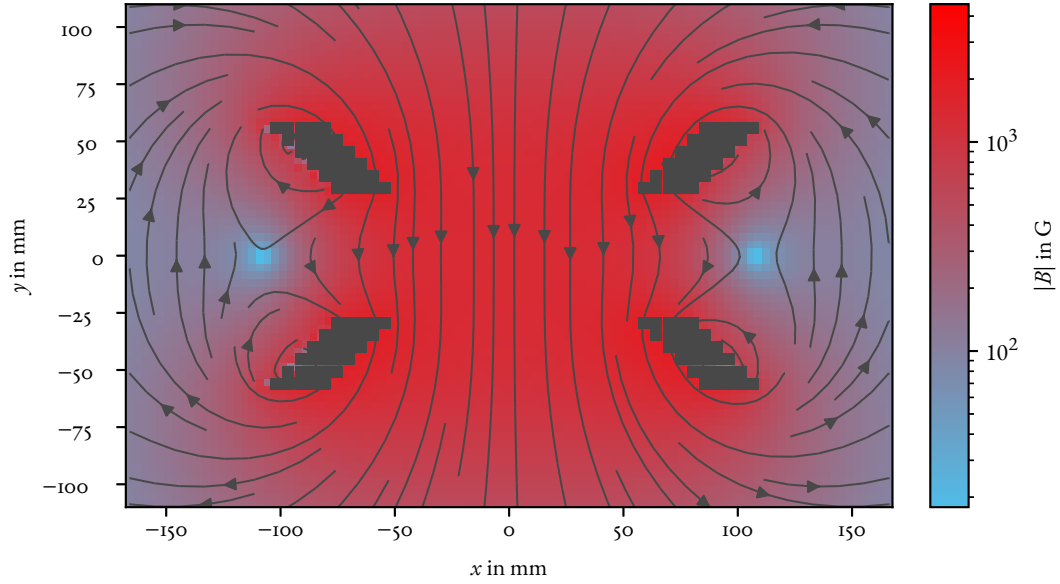
For this, the current of each was adjusted by the factor $\frac{\hat{r}^2}{(\hat{r}^2 + \hat{r}_0^2)^{\frac{3}{2}}}$ (cf. equation (4.17)) such that the fields in the center are equivalent:

$$\frac{I_{\text{optimal}, \text{Gauss}}}{I_{\text{optimal}, \text{Tesla}}} = \frac{\hat{r}_{\text{Tesla}}^2 / (\hat{r}_{\text{Tesla}}^2 + \hat{y}_{0, \text{Tesla}}^2)^{\frac{3}{2}}}{\hat{r}_{\text{Gauss}}^2 / (\hat{r}_{\text{Gauss}}^2 + \hat{y}_{0, \text{Gauss}}^2)^{\frac{3}{2}}} = \frac{400 \text{ A}}{396.5 \text{ A}} \quad (4.18)$$

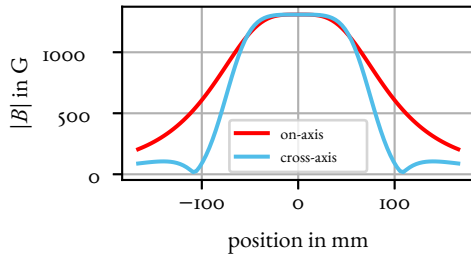
The positions of each coil were optimized in a grid-search way by varying them between 39.0 mm and 44 mm in steps of 0.5 mm, as shown in figure 4.12. Using sampled data from the fit model (4.17), the trap frequency due to the field curvature and the gradient were determined for each pair of positions using (4.13) and (4.14). The optimal positions found are listed in table 4.6. The positions of $y_{0, \text{Gauss}} = -41.0 \text{ mm}$ and $y_{0, \text{Gauss}} = 41.5 \text{ mm}$ are suggested to be used, as for these the trap frequency is minimal (0.63 Hz) and the gradient is almost negligible ($-0.07 \frac{\text{G}}{\text{cm}}$). Compared to the originally projected coil distance of about 85.5 mm, the optimal distance of $41 \text{ mm} + 41.5 \text{ mm} = 82.5 \text{ mm}$ is 3 mm more narrow.

The expected field landscape generated by *Gauss* and *Tesla* with optimized currents and positions is plotted in figure 4.13. At the time of writing of this thesis, the holder for the coils were not yet manufactured such that an experimental verification of this optimal configuration and further optimization is still pending.

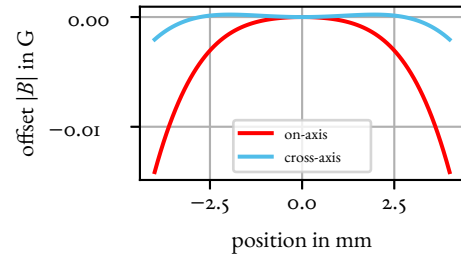
4. Feshbach and Gradient Field Coils



(a) Map of the Feshbach field at $I = 400$ A (the gray blocks are the windings' positions)



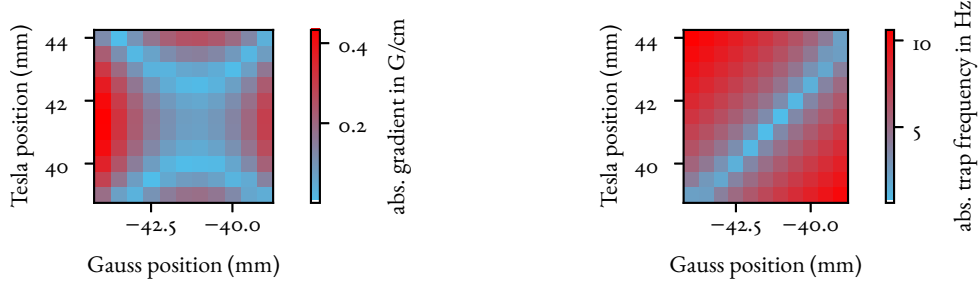
(b) Slices through the field landscape of the Feshbach field along the axis and along the cross-axis (radial) at $I = 400$ A



(c) Detail view of the center area of the projected size is the atomic cloud: The different curvatures in the axial and radial directions are discernible. Indicated field is relative to the field in the center.

Figure 4.11.: Simulated field landscape in Helmholtz/Feshbach configuration

4. Feshbach and Gradient Field Coils



(a) Expected absolute on-axis field gradient for different coil positions, calculated using (4.14) (b) Expected absolute on-axis trap frequency for different coil positions, calculated using (4.13)

Figure 4.12.: Optimization of the coil positions with respect to gradient and trap frequency: Using the fit parameters of the single coil measurements for *Gauss* and *Tesla* (see figure 4.9 and table 4.3), an expected field landscape was sampled from the model (4.17) for different coil positions (varied in 0.5 mm steps) from which gradient and trap frequency were calculated. Optimal positions are listed in table 4.6.

benchmark	optimal <i>Gauss</i> position	optimal <i>Tesla</i> position	optimum
on-axis gradient	−44.0 mm	+43.5 mm	0.00 $\frac{\text{G}}{\text{cm}}$
on-axis trap frequency	−41.0 mm	+41.5 mm	0.63 Hz

Table 4.6.: Expected optimal positions of the coils *Gauss* and *Tesla* for minimum trap frequency and gradient (see figure 4.12)

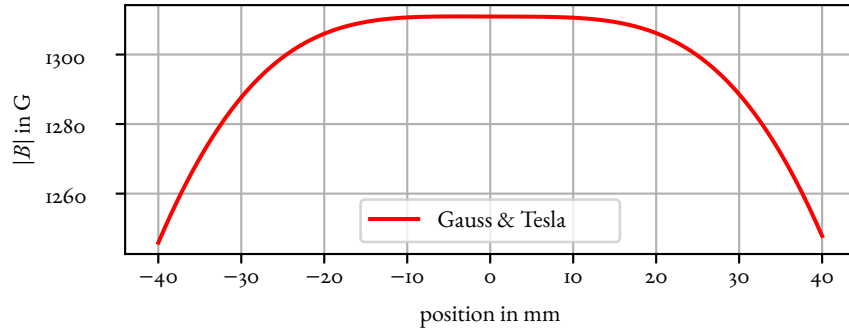


Figure 4.13.: Expected field landscape sampled from the field landscape model (4.17) for *Gauss* (left) and *Tesla* (right) with optimized positions $y_{0,Gauss} = -41.0$ mm and $y_{0,Tesla} = 41.5$ mm and optimized currents $I_{Gauss} = 400.0$ A, $I_{Tesla} = 396.5$ A. The resulting field landscape has a gradient of $-0.07 \frac{\text{G}}{\text{cm}}$ and a trap frequency of 0.63 Hz.

4. Feshbach and Gradient Field Coils

quantity	simulated value	equation reference
on-axis gradient per current	$0.49 \frac{\text{G}}{\text{cm A}}$	(4.14)
maximum on-axis gradient (± 400 A)	$197 \frac{\text{G}}{\text{cm}}$	
cross-axis/radial gradient per current	$0.25 \frac{\text{G}}{\text{cm A}}$	(4.14)
cross-axis/radial gradient (± 400 A)	$99 \frac{\text{G}}{\text{cm}}$	
inductance L_{cA}	0.10 mH	(4.10)
time constant τ_{cA}	6.5 ms	(4.11)
axial force (at 400 A) F_{cA}	105 N	(4.15)

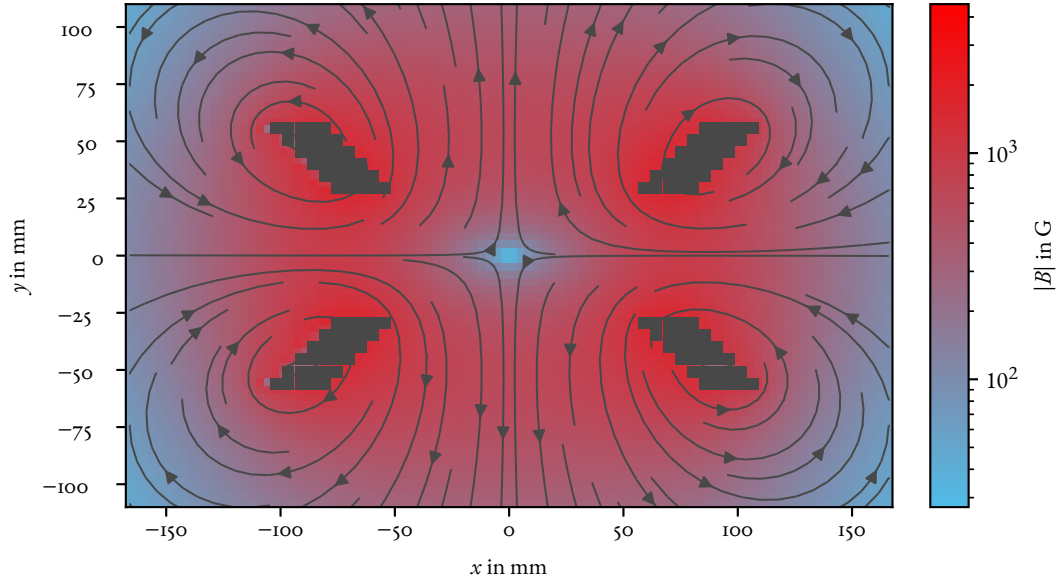
Table 4.7.: Properties of the coil arrangement in gradient configuration and of the produced fields (simulated using the *coil simulation library*). The gradient per current values refer to the linear components of the absolute field in a region of ± 3.5 mm around the center.

Magnetic Gradient

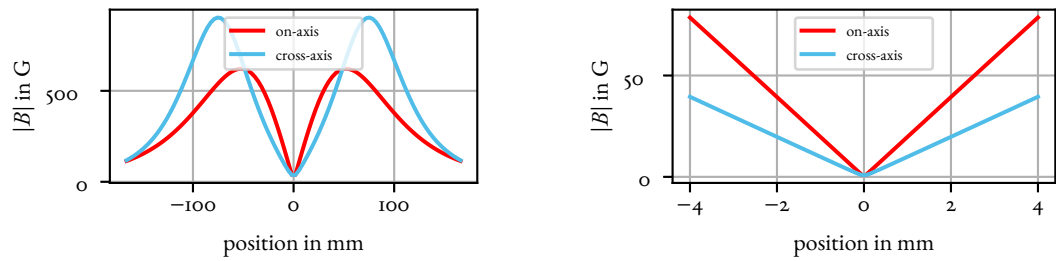
With the current inverted in one of the coils, a magnetic gradient field for the 3-dimensional magneto-optical trap can be generated. The field landscape is mapped in figure 4.14a, the gradients along the coil axis and the cross axis are displayed in figures 4.14b and 4.14c. At a full current of ± 400 A, gradients of $197 \frac{\text{G}}{\text{cm}}$ on the coil axis (y axis), and of up to $99 \frac{\text{G}}{\text{cm}}$ in radial direction (xz plane) in the trap region (± 3.5 mm) are in reach. Table 4.7 lists relevant properties of the gradient field.

Two handy rules of thumb have been formulated in the appendix chapter ?? for estimating the field and gradient in the center of a coil arrangement in Helmholtz configuration.

4. Feshbach and Gradient Field Coils



(a) Map of the gradient field at $I = \pm 400$ A (the gray blocks are the windings' positions)



(b) Slices through the field landscape of the gradient field along the axis and along the cross-axis (radial) at $I = \pm 400$ A

(c) Detail view of the center area of the projected size is the atomic cloud

Figure 4.14.: Simulated field landscape in gradient configuration

A. The Jones and Azimuth-Ellipticity Polarization Bases

using the Python library py-pol [36]. Note that py-pol defines $|R\rangle = \frac{1}{\sqrt{2}}(|H\rangle + i|V\rangle)$, $|L\rangle = \frac{1}{\sqrt{2}}(|H\rangle - i|V\rangle)$

B. Coil simulation library

C. Rules of Thumb for Magnetic Fields and Gradients

The following rules of thumb are useful for calculating the magnitude of homogeneous fields and gradients for coils in Helmholtz configuration, meaning that the distance of the coils equals their radius.

Homogeneous Fields

The field in Gauss at the center of a Helmholtz configuration of coils of radius r , distance r , operated at current I can be estimated as

$$B(r, I) \approx \frac{I}{1 \text{ A}} \left/ \frac{r}{1 \text{ cm}} \right. \cdot 1 \text{ G} . \quad (\text{C.1})$$

This means that, roughly speaking, coils in Helmholtz configuration generate a field of

$$1 \text{ G per } \frac{\text{A of current}}{\text{cm of radius}} .$$

Figure C.1 compares this rule of thumb to exact simulations with the *coil simulation library* (see 4.2 and B). The rule of thumb overestimates the field by about 10 %.

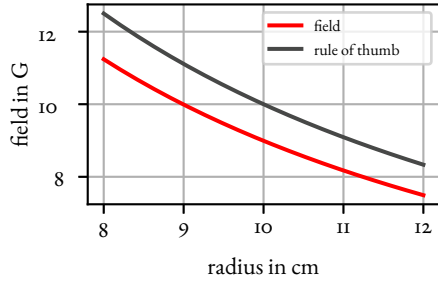
Gradient Fields

A similar rule of thumb can be formulated for the gradient around the center between coils in the same configuration, meaning the distance of the coils equals their radius, along the coil axis:

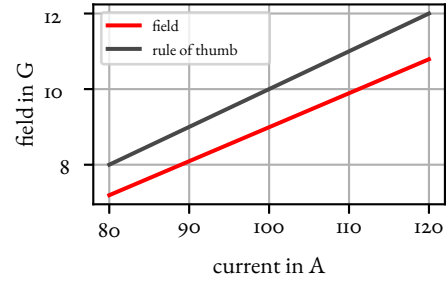
$$\frac{\partial B(r, I)}{\partial x_{\text{on-axis}}} \approx \frac{I}{1 \text{ A}} \left/ \left(\frac{r}{1 \text{ cm}} \right)^2 \right. \cdot 1 \frac{\text{G}}{\text{cm}} \quad (\text{C.2})$$

Figure C.2 compares the rule of thumb to simulations with the *coil simulation library* (see 4.2 and B). The rule of thumb underestimates the gradient by about 10 %.

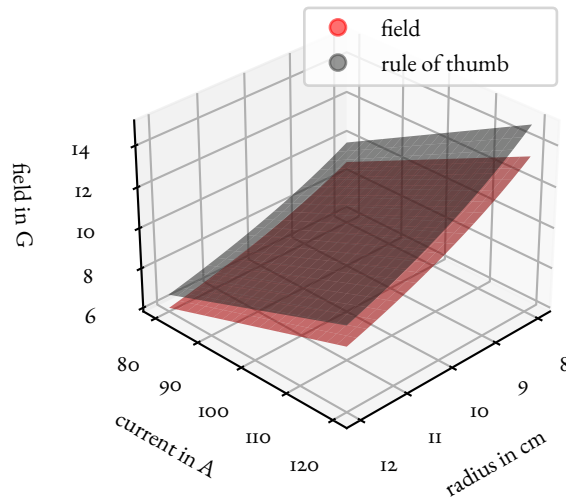
C. Rules of Thumb for Magnetic Fields and Gradients



(a) Dependency on the radius, with the coil distance fixed to the radius



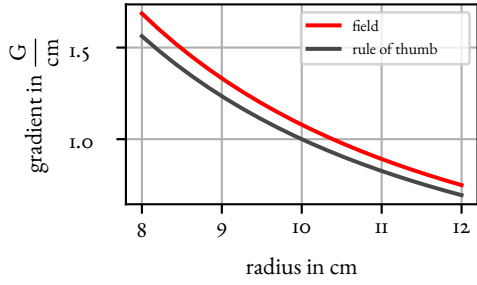
(b) Dependency on the current



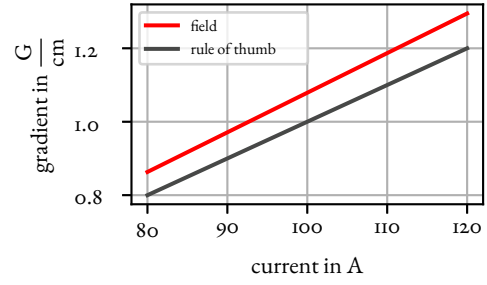
(c) Field as a function of radius and current: Exact fields are displayed in red, the rule-of-thumb approximation in gray above.

Figure C.1.: Fields in the center of a Helmholtz arrangement of coils for different radii and currents, comparing the rule of thumb (C.1) with simulated values. Parameters: $I = 100$ A, $r = 10$ cm, $N_{\text{windings}} = 1$

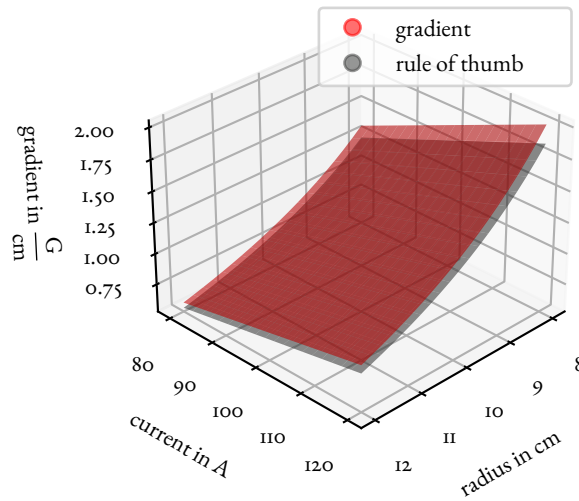
C. Rules of Thumb for Magnetic Fields and Gradients



(a) Dependency on the radius, with the coil distance fixed to the radius



(b) Dependency on the current



(c) Gradient as a function of radius and current: Simulated gradients are displayed in red, the rule-of-thumb approximation in gray below.

Figure C.2.: Gradients around the center of a Helmholtz arrangement of coils with mutually invert currents for different radii and currents, comparing the rule of thumb (C.2) with simulated values. Parameters: $I = 100$ A, $r = 10$ cm, $N_{\text{windings}} = 1$

References

- [1] C. J. Foot. *Atomic physics*. Oxford master series in physics 7. Atomic, Optical, and laser physics. OCLC: ocm57478010. Oxford ; New York: Oxford University Press, 2005. 331 pp. ISBN: 978-0-19-850695-9 978-0-19-850696-6.
- [2] Harold Metcalf and Peter van der Straten. *Laser Cooling and Trapping*. Springer, 1999. ISBN: 978-0-387-98728-6. URL: <https://link.springer.com/book/10.1007/978-1-4612-1470-0> (visited on 09/20/2022).
- [3] William Lunden et al. “Enhancing the capture velocity of a Dy magneto-optical trap with two-stage slowing”. In: *Phys. Rev. A* 101.6 (June 12, 2020), p. 063403. ISSN: 2469-9926, 2469-9934. DOI: 10.1103/PhysRevA.101.063403. URL: <https://link.aps.org/doi/10.1103/PhysRevA.101.063403> (visited on 11/11/2022).
- [4] T. G. Tiecke et al. “High-flux two-dimensional magneto-optical-trap source for cold lithium atoms”. In: *Phys. Rev. A* 80.1 (July 20, 2009). Publisher: American Physical Society, p. 013409. DOI: 10.1103/PhysRevA.80.013409. URL: <https://link.aps.org/doi/10.1103/PhysRevA.80.013409> (visited on 07/07/2022).
- [5] J. Kawanaka, K. Shimizu, and H. Takuma. “Decay rate measurement of lithium in a magneto-optical trap”. In: *Appl. Phys. B* 57.2 (Aug. 1, 1993), pp. 113–118. ISSN: 1432-0649. DOI: 10.1007/BF00425994. URL: <https://doi.org/10.1007/BF00425994> (visited on 10/14/2022).
- [6] P. M. Duarte et al. “All-optical production of a lithium quantum gas using narrow-line laser cooling”. In: *Phys. Rev. A* 84.6 (Dec. 21, 2011). Publisher: American Physical Society, p. 061406. DOI: 10.1103/PhysRevA.84.061406. URL: <https://link.aps.org/doi/10.1103/PhysRevA.84.061406> (visited on 07/07/2022).
- [7] Ahmed Omran et al. “Microscopic Observation of Pauli Blocking in Degenerate Fermionic Lattice Gases”. In: *Phys. Rev. Lett.* 115.26 (Dec. 23, 2015). Publisher: American Physical Society, p. 263001. DOI: 10.1103/PhysRevLett.115.263001. URL: <https://link.aps.org/doi/10.1103/PhysRevLett.115.263001> (visited on 10/06/2022).
- [8] U Schunemann et al. *Magneto-optic trapping of lithium using semiconductor lasers*. 1998. DOI: 10.1016/S0030-4018(98)00517-3. URL: <https://www.sciencedirect.com/science/article/pii/S0030401898005173> (visited on 07/07/2022).
- [9] Marc-Oliver Mewes et al. “Simultaneous magneto-optical trapping of two lithium isotopes”. In: *Phys. Rev. A* 61.1 (Dec. 8, 1999). Publisher: American Physical Society, p. 011403. DOI: 10.1103/PhysRevA.61.011403. URL: <https://link.aps.org/doi/10.1103/PhysRevA.61.011403> (visited on 07/08/2022).

References

- [10] F. Schreck et al. “Sympathetic cooling of bosonic and fermionic lithium gases towards quantum degeneracy”. In: *Phys. Rev. A* 64.1 (June 8, 2001). Publisher: American Physical Society, p. 011402. DOI: [10.1103/PhysRevA.64.011402](https://doi.org/10.1103/PhysRevA.64.011402). URL: <https://link.aps.org/doi/10.1103/PhysRevA.64.011402> (visited on 11/04/2022).
- [11] Timon Hilker. “Laser Cooling of Bosonic and Fermionic Lithium”. Diploma thesis. Technische Universität München, Physics Department, 2012.
- [12] Andreas Kerkmann. “A novel Apparatus for Quantum Gas Microscopy of Lithium Atoms”. Accepted: 2020-10-19T13:10:35Z Journal Abbreviation: Eine neue Apparatur für die Quantengasmikroskopie mit Lithiumatomen. PhD thesis. Hamburg: Staats- und Universitätsbibliothek Hamburg Carl von Ossietzky, 2019. URL: <https://ediss.sub.uni-hamburg.de/handle/ediss/6115> (visited on 10/14/2022).
- [13] Keith Ladouceur et al. “Compact laser cooling apparatus for simultaneous cooling of lithium and rubidium”. In: *J. Opt. Soc. Am. B, JOSAB* 26.2 (Feb. 1, 2009). Publisher: Optica Publishing Group, pp. 210–217. ISSN: 1520-8540. DOI: [10.1364/JOSAB.26.000210](https://doi.org/10.1364/JOSAB.26.000210). URL: <https://opg.optica.org/josab/abstract.cfm?uri=josab-26-2-210> (visited on 10/14/2022).
- [14] Y.-D. Chen et al. “Lithium-cesium slow beam from a two-dimensional magneto-optical trap”. In: *Phys. Rev. A* 103.2 (Feb. 8, 2021). Publisher: American Physical Society, p. 023102. DOI: [10.1103/PhysRevA.103.023102](https://doi.org/10.1103/PhysRevA.103.023102). URL: <https://link.aps.org/doi/10.1103/PhysRevA.103.023102> (visited on 10/14/2022).
- [15] Michael E. Gehm. *Properties of ^6Li* . Feb. 25, 2003. URL: <https://jet.physics.ncsu.edu/techdocs/pdf/PropertiesOfLi.pdf>.
- [16] Andrew T. Grier et al. “Lambda-enhanced sub-Doppler cooling of lithium atoms in D_1 gray molasses”. In: *Phys. Rev. A* 87.6 (June 12, 2013). Publisher: American Physical Society, p. 063411. DOI: [10.1103/PhysRevA.87.063411](https://doi.org/10.1103/PhysRevA.87.063411). URL: <https://link.aps.org/doi/10.1103/PhysRevA.87.063411> (visited on 10/12/2022).
- [17] A. Burchianti et al. “Efficient all-optical production of large $\text{Li } 6$ quantum gases using D_1 gray-molasses cooling”. In: *Phys. Rev. A* 90.4 (Oct. 8, 2014), p. 043408. ISSN: 1050-2947, 1094-1622. DOI: [10.1103/PhysRevA.90.043408](https://doi.org/10.1103/PhysRevA.90.043408). URL: <https://link.aps.org/doi/10.1103/PhysRevA.90.043408> (visited on 09/16/2022).
- [18] Kai Li et al. “Enhanced trapping of cold $\text{Li } 6$ using multiple-sideband cooling in a two-dimensional magneto-optical trap”. In: *Phys. Rev. A* 92.1 (July 22, 2015), p. 013419. ISSN: 1050-2947, 1094-1622. DOI: [10.1103/PhysRevA.92.013419](https://doi.org/10.1103/PhysRevA.92.013419). URL: <https://link.aps.org/doi/10.1103/PhysRevA.92.013419> (visited on 09/16/2022).
- [19] W. Scherf et al. “Re-measurement of the transition frequencies, fine structure splitting and isotope shift of the resonance lines of lithium, sodium and potassium”. In: *Z Phys D - Atoms, Molecules and Clusters* 36.1 (Mar. 1, 1996), pp. 31–33. ISSN: 1431-5866. DOI: [10.1007/BF01437417](https://doi.org/10.1007/BF01437417). URL: <https://doi.org/10.1007/BF01437417> (visited on 11/04/2022).

References

- [20] G. Grynberg and J.-Y. Courtois. “Proposal for a Magneto-Optical Lattice for Trapping Atoms in Nearly-Dark States”. In: *EPL* 27.1 (July 1994). Publisher: IOP Publishing, pp. 41–46. ISSN: 0295-5075. DOI: 10.1209/0295-5075/27/1/008. URL: <https://doi.org/10.1209/0295-5075/27/1/008> (visited on 10/12/2022).
- [21] M. Weidemüller et al. “A Novel Scheme for Efficient Cooling below the Photon Recoil Limit”. In: *EPL* 27.2 (July 1994). Publisher: IOP Publishing, pp. 109–114. ISSN: 0295-5075. DOI: 10.1209/0295-5075/27/2/006. URL: <https://doi.org/10.1209/0295-5075/27/2/006> (visited on 10/12/2022).
- [22] Manuel Gerken. “Gray Molasses Cooling of Lithium-6 Towards a Degenerate Fermi Gas”. In: (2016), p. 73. URL: https://www.physi.uni-heidelberg.de/Forschung/QD/datafiles/publications/theses/2016_Manuel_Gerken.pdf.
- [23] Janet Qesja. “Design of a 2-dimensional Magneto-optical Trap for a Fermion Quantum Processor”. Master’s thesis. Munich: Ludwig Maximilian University of Munich, Dec. 2022.
- [24] Robert G. Hunsperger. “Acousto-Optic Modulators”. In: *Integrated Optics: Theory and Technology*. Ed. by Robert G. Hunsperger. Advanced Texts in Physics. Berlin, Heidelberg: Springer, 2002, pp. 175–191. ISBN: 978-3-540-38843-2. DOI: 10.1007/978-3-540-38843-2_10. URL: https://doi.org/10.1007/978-3-540-38843-2_10 (visited on 11/04/2022).
- [25] *GaussianBeam*. SourceForge. URL: <https://sourceforge.net/projects/gaussianbeam/> (visited on 11/02/2022).
- [26] *Collimated Light’s Non-Zero Beam Divergence*. Apr. 20, 2021. URL: https://www.thorlabs.com/newgrouppage9.cfm?objectgroup_id=14489 (visited on 10/22/2022).
- [27] I. H. Malitson. “Interspecimen Comparison of the Refractive Index of Fused Silica*,†”. In: *J. Opt. Soc. Am., JOSA* 55.10 (Oct. 1, 1965). Publisher: Optica Publishing Group, pp. 1205–1209. DOI: 10.1364/JOSA.55.001205. URL: <https://opg.optica.org/josa/abstract.cfm?uri=josa-55-10-1205> (visited on 10/23/2022).
- [28] Wolfgang Demtröder. “Elektromagnetische Wellen in Materie”. In: *Experimentalphysik 2: Elektrizität und Optik*. Ed. by Wolfgang Demtröder. Springer-Lehrbuch. Berlin, Heidelberg: Springer, 2013, pp. 219–259. ISBN: 978-3-642-29944-5. DOI: 10.1007/978-3-642-29944-5_8. URL: https://doi.org/10.1007/978-3-642-29944-5_8 (visited on 10/23/2022).
- [29] David E. Pritchard. “Cooling Neutral Atoms in a Magnetic Trap for Precision Spectroscopy”. In: *Phys. Rev. Lett.* 51.15 (Oct. 10, 1983). Publisher: American Physical Society, pp. 1336–1339. DOI: 10.1103/PhysRevLett.51.1336. URL: <https://link.aps.org/doi/10.1103/PhysRevLett.51.1336> (visited on 10/30/2022).
- [30] Michael Hubertus Hagemann. “A Setup for High-Resolution Imaging of Ultracold Lithium Atoms”. PhD thesis. Hamburg: University of Heidelberg, 2020.

References

- [31] S Earnshaw. “On the Nature of the Molecular Forces which Regulate the Constitution of the Luminiferous Ether”. In: Transactions of the Cambridge Philosophical Society 7 (1842), p. 97. URL: <https://web.physics.ucsb.edu/~lecturedemonstrations/Linked%20files/Earnshaw.pdf>.
- [32] Michael Ortner and Lucas Gabriel Coliado Bandeira. “Magpylib: A free Python package for magnetic field computation”. In: *SoftwareX* 11 (Jan. 1, 2020), p. 100466. ISSN: 2352-7110. DOI: 10.1016/j.softx.2020.100466. URL: <https://www.sciencedirect.com/science/article/pii/S2352711020300170> (visited on 10/31/2022).
- [33] *magpylib/magpylib*. original-date: 2019-02-06T10:39:43Z. Oct. 19, 2022. URL: <https://github.com/magpylib/magpylib> (visited on 10/31/2022).
- [34] Wolfgang Demtröder. “Zeitlich veränderliche Felder”. In: *Experimentalphysik 2: Elektrizität und Optik*. Ed. by Wolfgang Demtröder. Springer-Lehrbuch. Berlin, Heidelberg: Springer, 2013, pp. 123–140. ISBN: 978-3-642-29944-5. DOI: 10.1007/978-3-642-29944-5_4. URL: https://doi.org/10.1007/978-3-642-29944-5_4 (visited on 11/05/2022).
- [35] Wolfgang Demtröder. “Statische Magnetfelder”. In: *Experimentalphysik 2: Elektrizität und Optik*. Ed. by Wolfgang Demtröder. Springer-Lehrbuch. Berlin, Heidelberg: Springer, 2013, pp. 83–121. ISBN: 978-3-642-29944-5. DOI: 10.1007/978-3-642-29944-5_3. URL: https://doi.org/10.1007/978-3-642-29944-5_3 (visited on 10/31/2022).
- [36] *Python polarization (py-pol)*. URL: <https://py-pol.readthedocs.io/en/master/> (visited on 10/24/2022).

Acknowledgements

Selbstständigkeitserklärung

Hiermit erkläre ich, diese Arbeit selbstständig verfasst und keine anderen als die in der Arbeit angegebenen Hilfsmittel verwendet zu haben.

München, den . Dezember 2022

insert date

Tobias Maximilian Philipp Schattauer